CALICE Analysis Note 001
July 3, 2007

Study of the response of the CALICE silicon-tungsten electromagnetic calorimeter prototype to electrons

The CALICE Collaboration [1]

Abstract

A prototype Silicon-Tungsten electromagnetic calorimeter for an ILC detector was installed and tested during summer 2006 at DESY, and subsequently operated at the CERN SPS test beam. The detector consisted of 6480 1x1 cm^2 silicon pads. Data were collected with electron and hadron beams in the energy range 1 to 50 GeV. The analysis described here focuses on electromagnetic shower reconstruction. This analysis is crucial in order to demonstrate the quality of the calibration and understanding of the detector through comparison with Monte Carlo simulations. In subsequent analyses, the data will be combined with those recorded with the Calice analogue HCAL and tail catcher (TCMT) in order to study hadronic showers with high spatial precision.

[1]Corresponding author: D.R. Ward; drw1@cam.ac.uk

Contents

1 Introduction

The current designs of the calorimetry for detectors at the ILC are in large part driven by the demands of jet energy reconstruction. A key aim is to achieve a relative energy resolution of $\sim 30\%/\sqrt{E/\mathrm{GeV}}$; this precision would for example permit the reconstruction of the hadronic decays of the W and Z bosons with a precision comparable with their natural widths, and would allow the W and Z to be distinguished in their hadronic (two-jet) decay modes.

The target of $\sim 30\%/\sqrt{E/\mathrm{GeV}}$ jet energy resolution is roughly a factor two better than achieved in previous detectors. The way to achieve it is believed to be through "*particle flow*". The idea is that particles of different types in jets should be reconstructed in the different parts of the detector where they can be measured most precisely: the charged particles in the tracking system, photons in the electromagnetic calorimeter (ECAL) and neutral hadrons in the hadronic calorimeter (HCAL). The key to this concept is the pattern recognition in the calorimeters, and to achieve this, high spatial granularity is required. This is more important than the intrinsic energy resolution for single particles.

The optimum design of the ILC detectors can be addressed by Monte Carlo simulation, but in order to do this, it is crucial to validate the Monte Carlo tools against data. The aims of the CALICE beam test program are therefore twofold:

- To construct realistic prototype calorimeters and test their operation in beam tests.
- To confront the data with Monte Carlo simulations of the same kind as used for the full detector. This is especially important in the case of hadronic showers, where models are notoriously unreliable.

The CALICE plan is to expose complete calorimeter system (ECAL, HCAL and muon system using various technologies) to test beams of electrons, muons and hadrons. To this end, a first round of beam tests was performed at DESY and CERN in summer 2006. In this note we summarise some of the **preliminary** results from the ECAL; in companion notes we report on the other detectors tested.

2 The Calice Prototypes

The ECAL prototype is made of 30 readout layers. The mechanical structure is built from tungsten sheets wrapped in carbon fibre. The active detectors are silicon diode wafers segmented into pads with a size of 1×1 cm^2. The very front end (VFE) electronics provide preamplification and are located outside the active area, but mounted on the same PCB as the silicon wafers. This PCB is then connected via cables to VME readout electronics which provide digitisation and readout. The prototype is built of three stacks, each of ten layers of alternating tungsten and silicon, each stack having a different tungsten thickness:

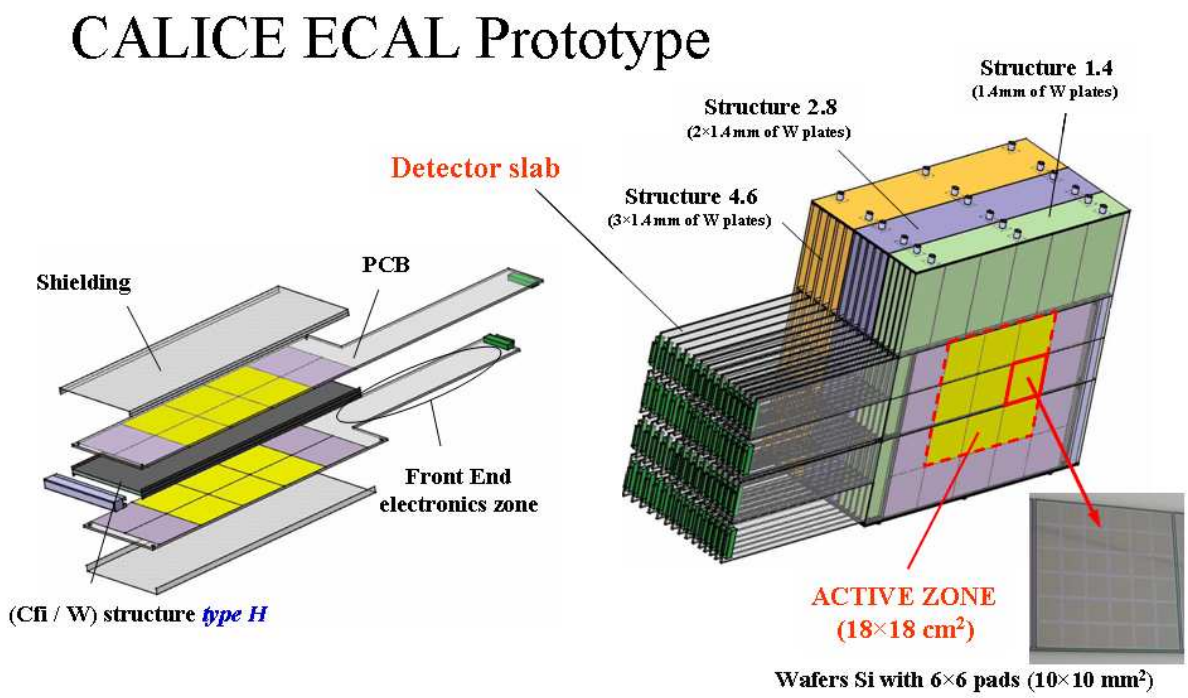

Figure 1: *General layout of the Calice Si-W ECAL prototype.*

1.4 mm or $0.4X_0$ per layer in the first stack, 2.8 mm or $0.8X_0$ per layer in the second stack and 4.2 mm or $1.2X_0$ per layer in the rear stack. This choice should ensure a good resolution at low energy, due to the thin tungsten in the first stack, combined with a good containment of the electromagnetic showers. The overall thickness is about 20 cm or $24X_0$ at normal incidence. These three stacks are mechanically separate. The calorimeter is designed to be rotated to angles 10°, 20°, 30° and 45° with respect to the beam; when this is done, the stacks are translated laterally so that the beam still passes through all three stacks. A sketch of the general layout of the prototype is given in Fig. 1.

The structure was constructed by wrapping half of the tungsten sheets in carbon fibre, leaving free spaces (called *alveoli*) between each tungsten sheet. Detector slabs are inserted into the alveoli. Each detector slab consists of two active silicon layers on either side of a tungsten sheet. Each active layer is made of a PCB (14 layers, thickness 2.1 mm) and up to six high resistivity silicon wafers (thickness 500μm). The wafers were cut to a size of 62×62 mm^2 which contains an array of 6×6 pads, each 10×10 mm^2, with a space reserved for the guard ring of about 1 mm. The wafers are operated in over-depleted mode at a potential of around 200 V. The wafers on either side of a detector slab are staggered by 2.5 mm in the horizontal (x) direction, in order to avoid aligning the guard ring gaps., and successive slabs within a stack are similarly staggered by 1.3 mm. The guard rings in the vertical (y) direction are aligned. The layout of one of the PCBs is shown in Fig.2.

The full prototype will consist of a 3×3 array of wafers in each layer. The prototype

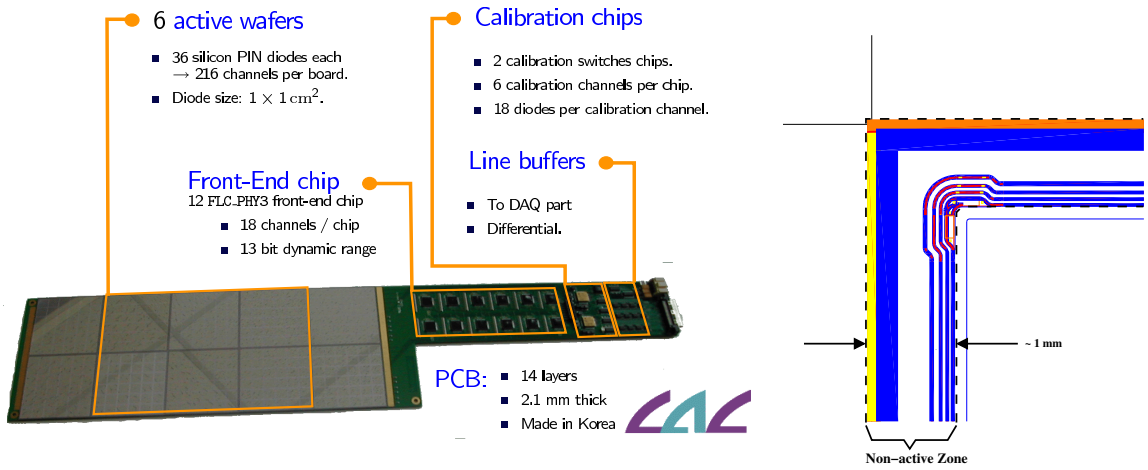

Figure 2: *Structure of an ECAL readout PCB. The guard ring structure is indicated on the right.*

tested at CERN in 2006 consisted of 30 layers, each instrumented by a 3×2 array (i.e. an instrumented area of 18×12 cm^2). This should be amply adequate for transverse containment of electromagnetic showers. The prototype tested at DESY consisted of 30 layers of tungsten, but only 24 of the silicon layers, placed after each of the first 22 tungsten plates, and after the 25$^{\text{th}}$ and 26$^{\text{th}}$ plates.

The silicon wafer diodes are read by a VFE chip, consisting of a preamplifier with two gains, a shaper and a multiplexer. Each chip handles 18 channels and has low noise and a large dynamic range. The front end electronics was read out using custom-designed 9U VME boards, each capable of handling handling up to 1728 channels. The readout boards contain 16 bit, 500 kHz ADCs for digitisation and an 8 MByte buffer for data storage during a spill. All data from these detectors can be digitised and stored on board in less than 100μs after the trigger.

3 Test Beam Setup

In May 2006 the Calice ECAL prototype was tested on electron beams at the test beam 21 area at DESY. A sketch of the test beam setup is shown in Figure 3. The beam trigger is defined by the coincidence signal of three scintillator counters (Sc1, Sc2 and Sc3). The size of the beam is defined by two scintillator counters, mounted in T shape (Fc1 and Fc2). The resulting e$^-$ beam spot is roughly 7×5 mm^2 at the calorimeter at a beam energy of 6 GeV. Four drift chambers (DC1, DC2, DC3 and DC4) are used to monitor the beam. Fig. 4 shows the ECAL in the DESY beam, and Fig. 5 shows a larger view including the drift chambers.

Various scans were performed in order to characterise the prototype:

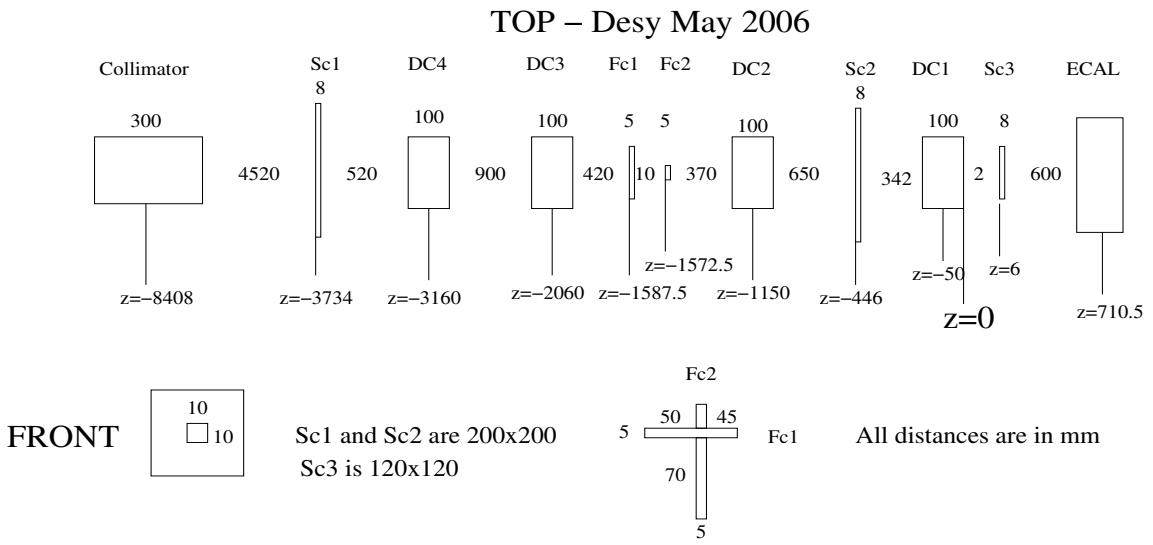

Figure 3: *Sketch of the DESY test beam setup in May 2006.*

- e^- beams from 1 to 6 GeV were used to study linearity and resolution;
- e^- beams from 1 to 6 GeV were sent to the centre, edge and corner of the wafers to study effects such as shower shape and energy leakage;
- the ECAL prototype was rotated by 10, 20, 30 and 45 degrees with respect to the beam direction to study the angle effects on the resolution.

Over 8 million triggers were collected, as detailed in Table 1. All events were reconstructed using Marlin [1], converted to a standard LCIO [2] format and are available in the DESY dcache repository (`http://www.dcache.org`).

Angles(deg)	0 (kEvt)	10 (kEvt)	20 (kEvt)	30 (kEvt)	45 (kEvt)
6 GeV	594	688	200	185	200
5 GeV	304	300	200	325	200
4 GeV	400	224	200	300	200
3 GeV	304	200	200	324	200
2 GeV	400	200	200	300	200
1.5 GeV	486	200	200	300	200
1 GeV	400	300	345	200	200
Total	2888	2112	1545	1934	1400

Table 1: *Summary of the events collected at the DESY test beam.*

In August and October 2006 a combined ECAL-HCAL-TCMT test beam was carried out at the H6 area at CERN, using electron and pion beams. Sketches of the beam lines as simulated are presented in Figure 6 and 7. The beam trigger was defined by the

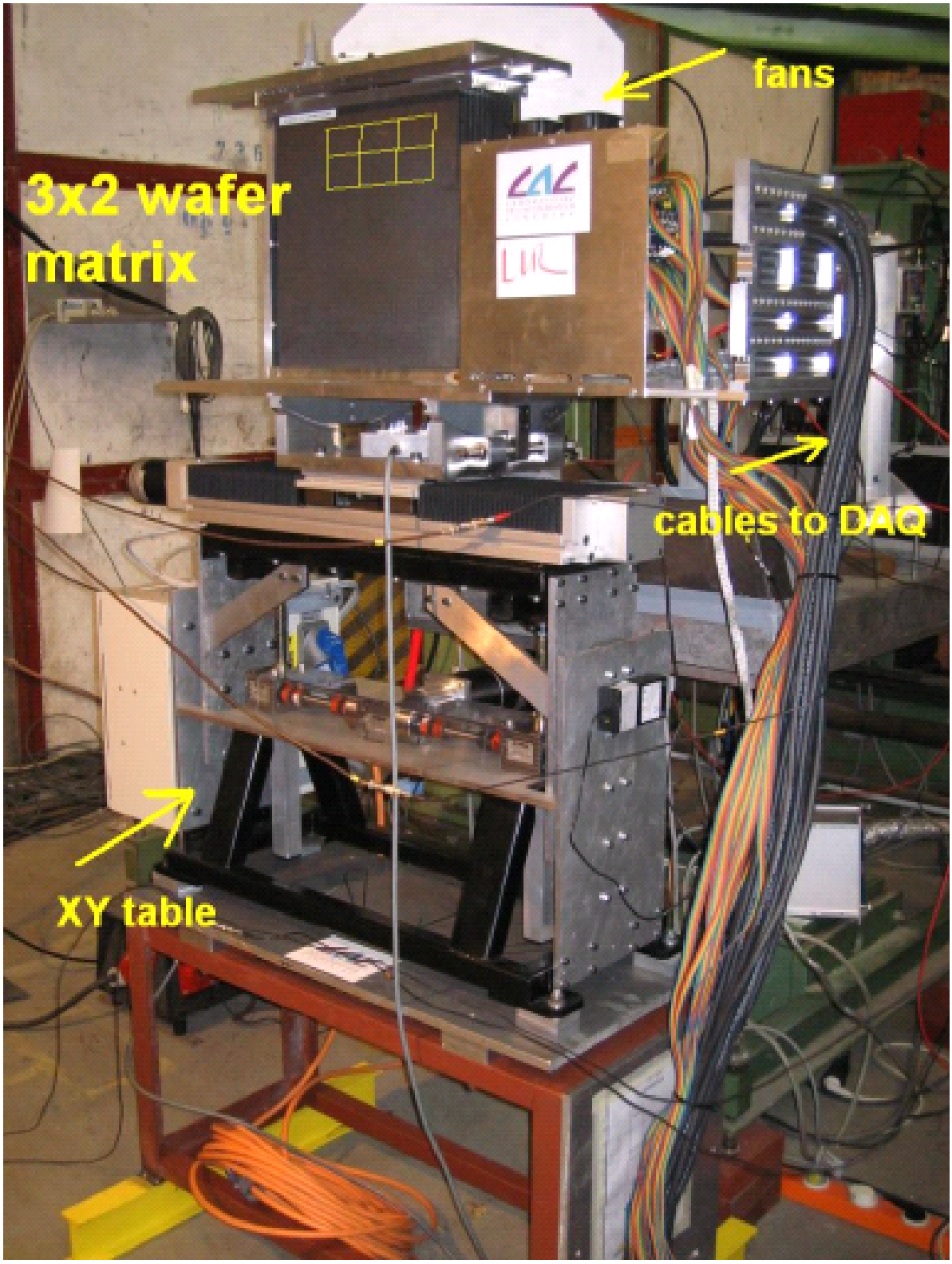

Figure 4: *The Calice ECAL in the DESY test beam.*

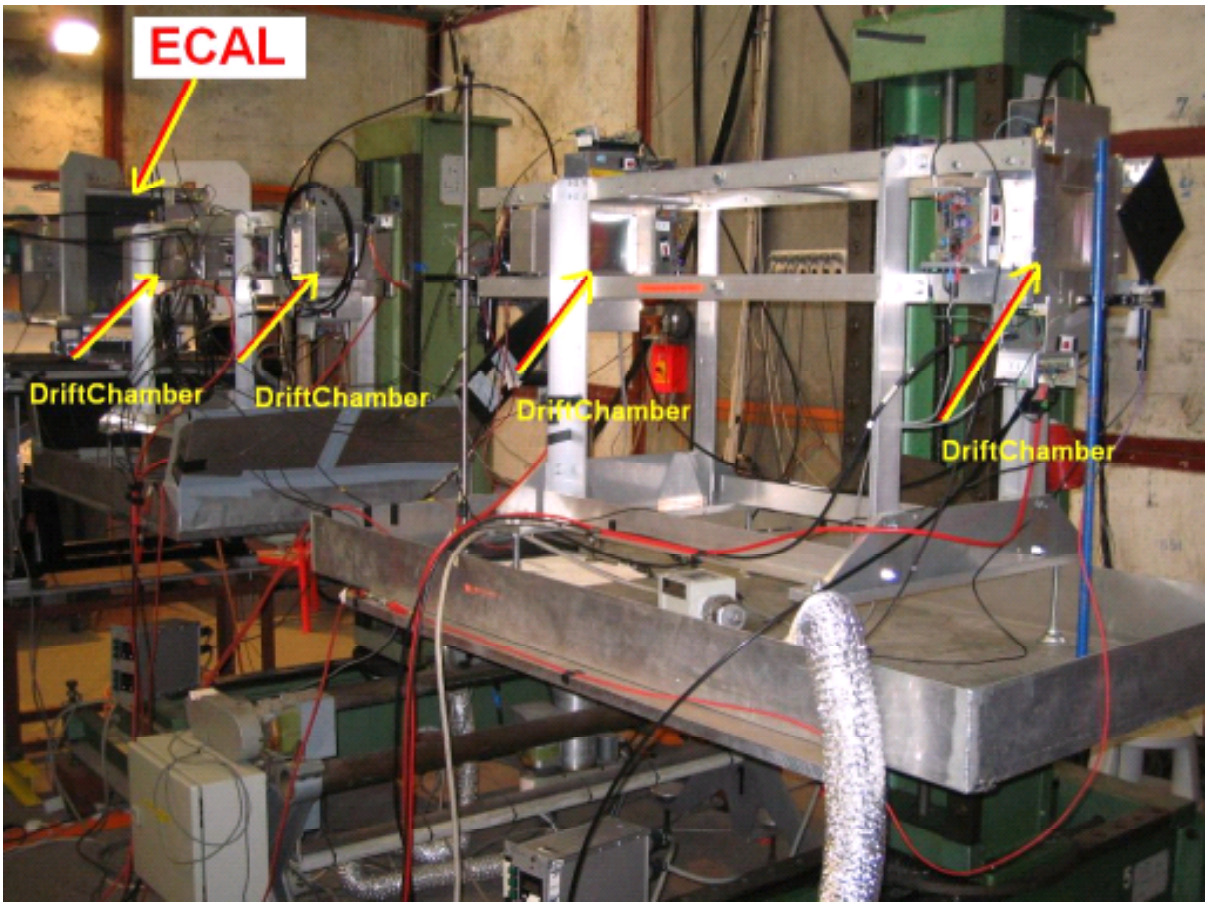

Figure 5: *The general layout in the DESY test beam.*

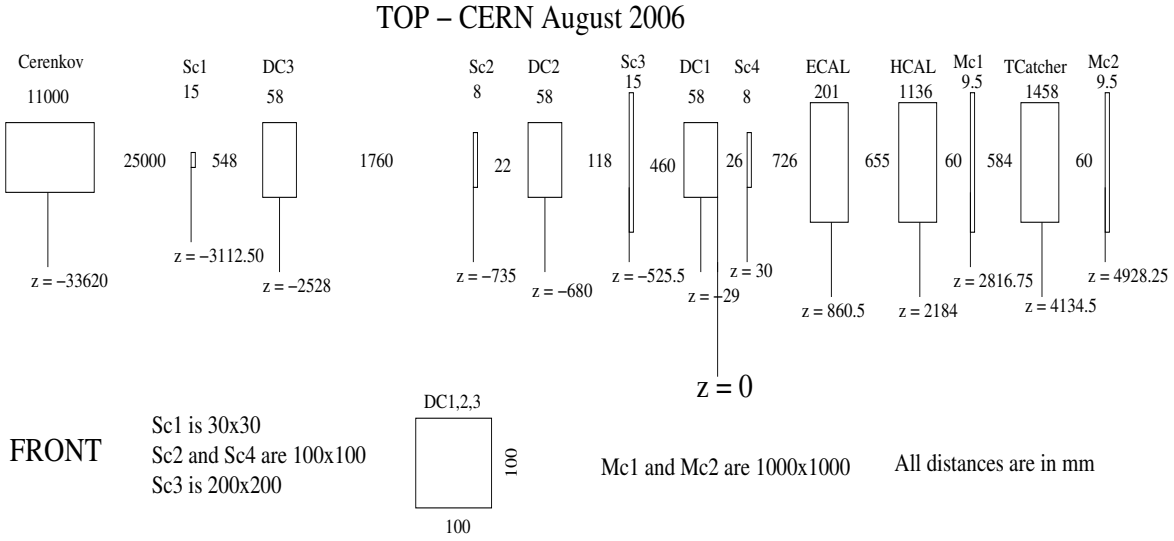

Figure 6: *Sketch of the CERN test beam setup in August 2006.*

coincidence signal of three scintillator counters (Sc1, Sc2 and Sc4 in the August setup, Sc1, Sc2 and Sc3 in the October setup). The beam halo is vetoed with a scintillator counter (Sc3 in August, Sc4 in October). Three delay wire chambers (DC1, DC2, DC3) [3] are used to monitor the beam. A Cerenkov detector is used to separate electrons from pions. Muons are identified by two scintillators (Mc1, Mc2) placed behind the HCAL prototype.

During the August runs the TCMT detector was not present, so only ECAL and HCAL were tested. Several different run conditions were used, as detailed below:

- ECAL alone: e^- beams from 10 to 45 GeV were used to complement the linearity and resolution studies carried out at the DESY test beam. Angle effects on the resolution were also studied by rotating the ECAL prototype by 20, 30 and 45 degrees with respect to the beam direction. A summary of the total events collected in this first period is given in Table 2.
- HCAL alone: e^- beams from 6 to 45 GeV and π^- beams from 6 to 80 GeV were used to study linearity and resolution;
- a combined ECAL+HCAL test were carried out using π^- beams from 30 to 80 GeV. A summary of the total events collected in this period is given in Table 3.

In addition, 30 million muon events were collected for calibration purposes.

In the October running the TCMT detector was installed on the beam line and one muon chamber (Mc2) was removed. The layout of the detectors at this time is shown in Fig. 8. Also in this case, several different run conditions were used:

- ECAL alone: e^+ and e^- beams from 6 to 50 GeV;

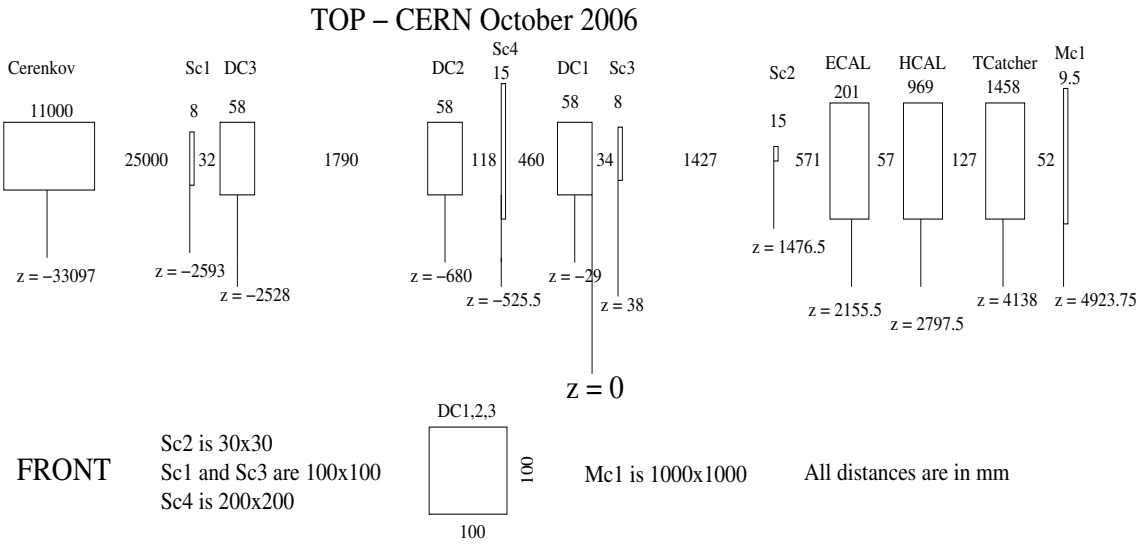

Figure 7: *Sketch of the CERN test beam setup in October 2006.*

Angles(deg)	0 (kEvt)	10 (kEvt)	20 (kEvt)	30 (kEvt)	45 (kEvt)
45 GeV	933		250	753	551
40 GeV	347			280	311
30 GeV	685		270	550	531
20 GeV	380		110	330	208
15 GeV	201			181	244
10 GeV	297		112	594	530
Total	2843		742	2688	2375

Table 2: *Summary of the events collected in the ECAL only period in the August CERN test beam.*

- HCAL alone: e^+ and e^- beams from 6 to 50 GeV;
- ECAL+HCAL+TCMT: π^+ and π^- beams from 6 to 80 GeV.

A summary of the electron and pion runs collected is given in Table 4. In addition, more than 27 million muon events were collected. An event display of a typical electron shower in the ECAL is shown in Fig. 9. The data were converted into LCIO and subsequently reconstructed using a series of Marlin processors. Conditions Data like e.g. temperatures and detector donfigurations are stored in a MySQL database which is operated at DESY. All data files are available via grid tools. For the data management and processing using the grid the virtual organisation `calice` has been established which currently has 45 members.

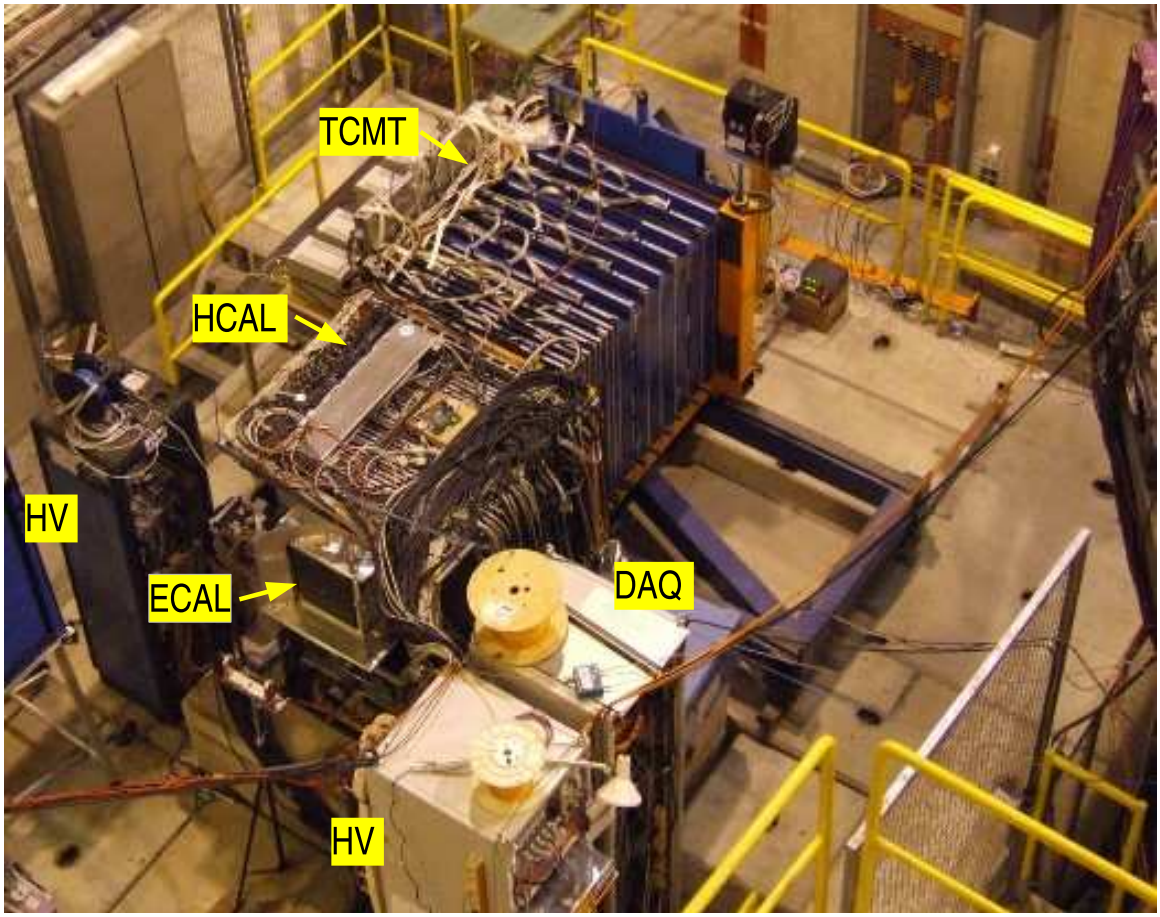

Figure 8: *Layout of the three Calice calorimeters at CERN in October 2006.*

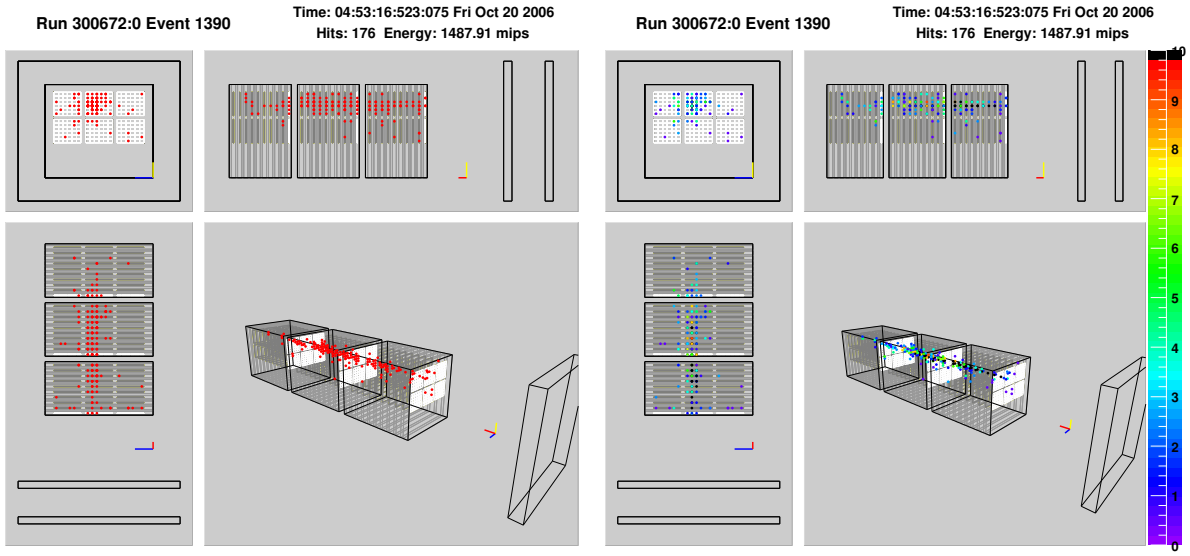

Figure 9: *A typical 10 GeV e^- shower in the electromagnetic prototype. The detector cells with signal above 0.5 mip threshold are displayed. (Layout not to scale)*

Angles(deg)	0 (kEvt)	10 (kEvt)	20 (kEvt)	30 (kEvt)	45 (kEvt)
80 GeV	92				
60 GeV	46			433	
50 GeV	143			359	
40 GeV	210				303
30 GeV	129			47	
Total	620			839	303

Table 3: *Summary of the events collected in the ECAL+HCAL period in the August CERN test beam.*

	e^+ (kEvt)	e^- (kEvt)		π^+ (kEvt)	π^- (kEvt)
6 GeV	208	128		480	1800
8 GeV		218			1800
10 GeV	152	172		960	1800
12 GeV		211			1600
15 GeV	476	124		720	1600
16 GeV	310				1700
18 GeV	303	231		770	1600
20 GeV	390	210		3300	
30 GeV	409			1400	
50 GeV	305			1500	
80 GeV				1800	

Table 4: *Summary of the events collected in the ECAL+HCAL+TCMT period in the October CERN test beam.*

4 ECAL Calibration

4.1 Gain Calibration

4.1.1 Data set for Calibration

The current calibration of the ECAL prototype has been performed by using a set of 74 high-statistics muon runs ($\sim$ 250000 events each). All those runs were taken during October 2006 with another experiment upstream providing a wide spread of the muon beam over all the surface of the prototype. Therefore events were triggered with a 1 m^2 scintillator counter.

4.1.2 Procedure

After pedestal subtraction (sect. 4.2), the runs are then reconstructed using a fixed global noise cut of 25 ADC counts which corresponds to one half of the rough calibration constant of 50 ADC counts estimated in former studies, so that the individual calibration constants are obtained as fractions of 50 ADC counts. MIP values given in the following should therefore be understood in this scale of 1 MIP=50 ADC. To reject any remaining noise hits, it is required that the hits of one event form tracks of minimum ionising particles (MIPs). To achieve this, basically two criteria are applied:

- number of reconstructed hits in the track ≥ 15 and ≤ 40
- distance between two hits i and j fulfils: $\sqrt{(x_i - x_j)^2 + (y_i - y_j)^2} \leq 2\text{cm}$

From the hits of these tracks a signal histogram is built for every channel of the prototype. Since the muon spread was not totally uniform over the whole surface, the entries of the histograms vary from a few thousand in the border regions to up to 14000 in the centre part. The distribution obtained should ideally be described by a convolution of a Gaussian and a Landau function. Such a function is therefore used to fit the data. The most probable value (MPV) of the Landau function would then give the calibration constant while the standard deviation of the Gaussian would give the noise value for each cell. The high statistics caused the emergence of a small bump at around 2 MIP, which can be explained by the emission of δ-rays. To avoid any disturbance of the fitting by this effect the fitting range has been limited to the range between 0 and 1.57 MIP.

4.1.3 Results

For 6403 of the 6480 channels of the prototype a calibration constant could be obtained via this method without further intervention. 32 of the remaining cells showed a noise value that was unusually high so that the fit did not converge. In order to obtain a value nevertheless we fitted a Gaussian function in the range of 0 up to the start of the mip peak in order to estimate the additional noise. Then we subtracted this function from the original signal histogram. The distributions of 18 channels could be cleaned like this and then be refitted. For the remaining 14 the noise contribution was so high that a Gaussian fit could not be applied. These cells were calibrated by copying the calibration constant from one of their neighbours.

One entire wafer seemed to show no MIP peak at all. In an additional test using cosmic muons it was discovered that its signal output is about half the value of the other wafers. The cause of this, as it was later identified, is that the wafer seems not to be fully depleted at the applied voltage of 200V. Although no absolute values could be obtained in this test because a different DAQ system has been used, a relative value between the mean MIP signals of the wafer in question and its neighbour could be estimated to be 0.517, allowing a relative calibration of the cells.

Eight cells gave no output and were considered as dead. The one remaining cell had to be declared as dead as well since it showed a strange signal histogram probably due to a problem with the preamplifier.

This leaves 9 out of 6480 channels without a valid calibration constant. The calibration constants for all calibrated channels are histogrammed in Fig. 10. The distribution is narrow, with almost all pads in the range 40–50 ADC counts/MIP. The small peak at 23.5 corresponds to the single incompletely depleted wafer.

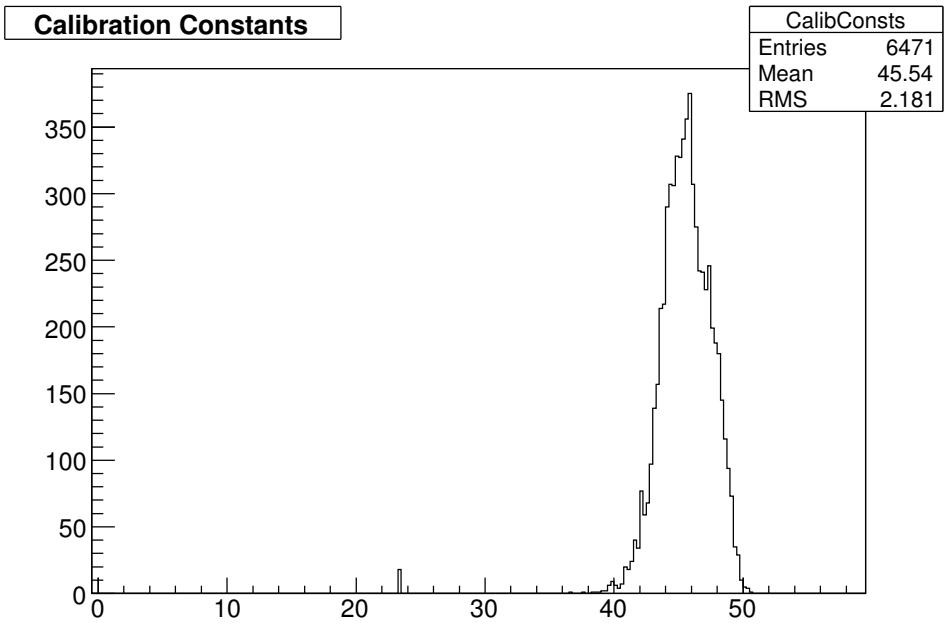

Figure 10: Equivalent ADC value for the energy deposit of 1 MIP for the live cells of the ECAL prototype

4.2 Pedestals

4.2.1 Extraction procedure

For all beam tests performed, the data acquisition consisted of a fixed sequence of 500 pedestal events, 500 events with charge injection via the calibration chips and then 20000 beam events. This cycle is then repeated until the end of the run. During the first 500 pedestal events, it is assumed that no hits are seen in the detector. So all the raw ADC values for one cell are accumulated. In case of hits in the detector pedestal and noise would thus be shifted to bigger values. To perform a minimal rejection of eventual hits or big fluctuations the maximum ADC value for each cell in a block of 20 events is not taken into account for the final calculation. The pedestal is than given by the mean of this values, the noise by the RMS. In the pedestal events of the following cycles an effective

hit rejection can be applied. Since a pedestal and noise value are known from the initial calculation, one can use a simple cut to define a hit. In the current reconstruction a cell is called hit when its pedestal-subtracted ADC value exceeds 5 times its noise value. The recalculation of the pedestal is now performed via the change in respect to the last calculation in order to detect big pedestal shifts.

4.2.2 Pedestal instabilities

It has been observed that the pedestals are not necessarily stable. This effect is PCB wide. It concerns several particular PCBs and is time dependant. For these PCBs, the pedestals are not constant in time as assumed, but subject to a random shift affecting all channels of one layer with the same drift. Some of the PCBs affected at DESY then behaved normally again at CERN. This effect is attributed to the instabilities of the power supplies giving the pedestal lines, which were not isolated at this time.

The basic idea to correct for these instabilities of the pedestals is to try and recalculate them event by event. For every layer, first any wafers showing a hit are excluded from this recalculation. Since the normal hit cut cannot be applied a wafer with a hit is defined by a minimum difference of the minimal and maximal ADC value of its cells, this limit being 3000 ADC counts. This technique is thus safe for the occupancies given in a single particle beam. An iterative procedure is than applied using the cells of the remaining wafers to calculate the new pedestal until its RMS is of the order of the mean noise of the PCB. The new pedestal is stored to be the basis for the next event.

4.3 Noise

4.3.1 Coherent noise and crosstalk

The following study is based on a particular run (230101), taken with 6 GeV electrons, and with statistics of 100,000 triggers. It has been checked that most of the observed features are PCB (or Wafer, or even channel) dependant, but sometimes also time dependant.

We can classify the effects observed up to now in three categories :

- Coherent noise : this is the pedestal instabilities described above. This will be referred to as "global corrections" in the following, as the calculated pedestal shift is applied to the whole PCB.
- Crosstalk in all the cells of some wafers recording a high signal. The effect is seen as a pedestal shift towards negative values , for all the channels of the wafer recording a signal, but not for neighbouring wafers. This seems to be random, on some particular wafers, but not constant in time. We observe anyway a clear

correlation of this effect with the intensity of the signal recorded. It will be called the Signal Induced Pedestal Shifts (SIPS) effect in the following. This effect is not yet understood but under investigation. In order to correct for this effect, the mean and standard deviation is calculated on an event-by-event basis, per wafer, after discarding the signal hits, and iterating on the channels taken into account in the sum.

- Finally, some cells are intrinsically strongly (anti)correlated, independently of the time. This effect will be simulated.

In order to identify and characterise these effects, the correlation between pairs of channels has been calculated in signal events, after each step of the corrections. No clear correlation is seen in an entire PCB, except the one coming from the pedestal drift. We will thus show only the results wafer by wafer.

- Figures 11, 12-17, 19 shows the correlation factors (colour scale) as a function of the two channel indices, numbered from 0 to 35, row by row (6*pad_column+pad_row). So channels numbered 0-17 belong to one chip, and 18-35 correspond to the other chip. The corresponding noise level per layer, for all wafers, is also presented in figures 11 bottom-right, 18, and 20. The correlations are shown before any correction, after global pedestal shift correction, and after Signal Induced Pedestal Shift corrections.
  Figure 11 shows a typical layer with no particular problem. The 3×3 pattern observed just reflects the way the calibration lines are wired. The same pattern is seen in the noise distribution (bottom-right plot), confirming there is a small anticorrelation between the left and the right part of both chips.

- Figures 12 shows a layer affected by the global pedestal drift, before and after the global corrections. Corrections here remove entirely the 50% coherent noise. Two particular cells remains almost 90% anticorrelated.

- Figures 13 to 16 show a layer affected by the global pedestal drift, and by the SIPS (figures 17). The beam was directed in module 3, stave 2,[2] and it can be seen that the region affected by the signal shows less correlation, due to the fact that most pixels are discarded in the noise calculation because they record a signal. The global corrections are anyway still doing their job really well, removing about 6 ADC counts of coherent noise on top of the normal noise level of 6 ADC counts, see figure 18. A remaining correlation of about 20% can still be observed after the SIPS corrections (figure 17, right).

- Figures 19 and 20 shows a layer affected only by the SIPS in the wafer recording signal hits. The corrections are seen giving a really nice result here, going down to a level of 2% correlations.

[2]The term "module" (2 or 3) refers to a row of wafers in the ECAL, and "stave" (1 to 3) refers to the wafer index within the row.

Having global pedestal shift on top of the SIPS seems to affect the quality of the corrections. These corrections will be quantified and studied using the Monte Carlo simulation in the near future.

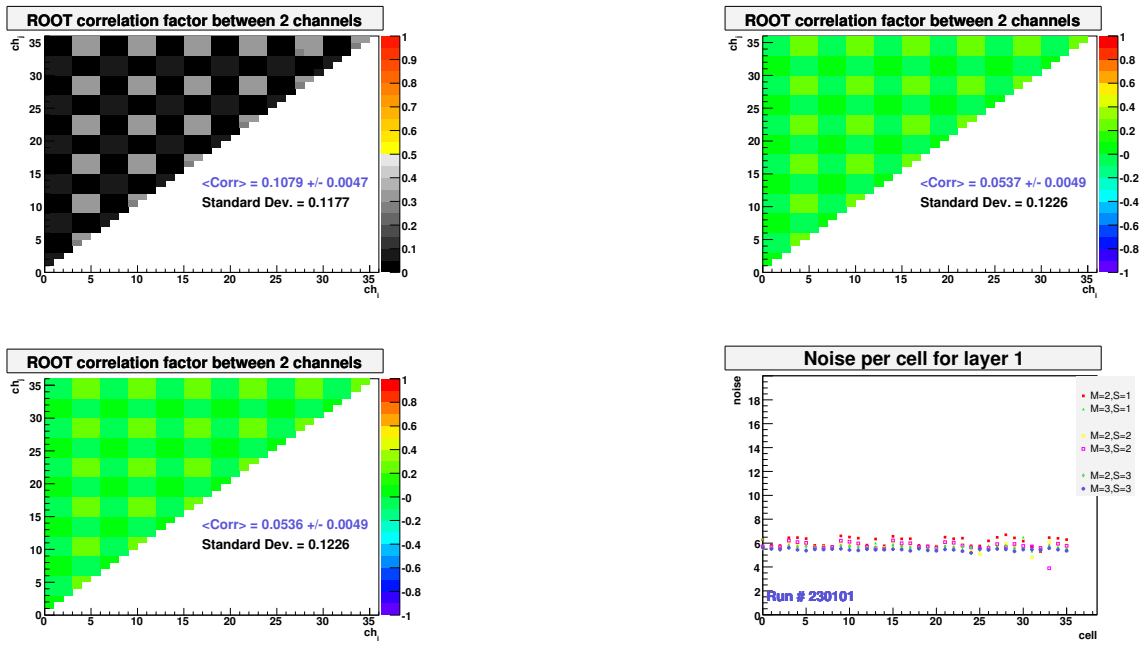

Figure 11: Layer 1, stave 1, module 2, up-left: before any corrections, up-right: after global corrections, bottom-left: after global and SIPS corrections, and bottom-right: mean noise observed per wafer after all corrections.

Figure 12: Layer 7, stave 2, module 2, before any corrections and after global corrections.

4.3.2 Noise measures

Two procedures have been applied to extract the mean noise values for the cells of the prototype:

- extraction from the width of the MIP peak in the muon data used for the gain calibration

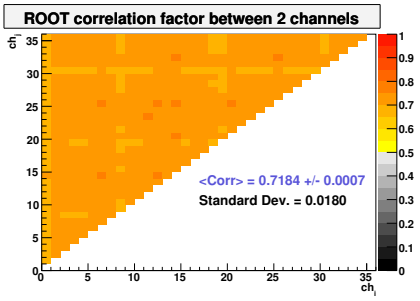

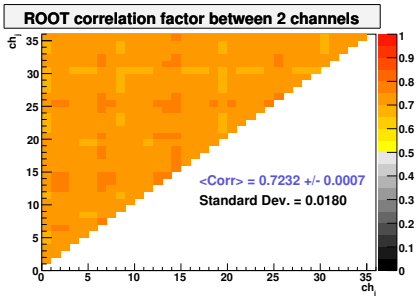

Figure 13: Layer 8, stave 1, left: module 2, before any corrections, right: module 3, before any corrections.

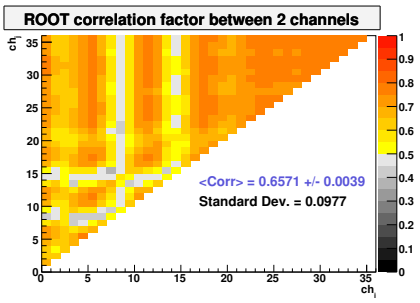

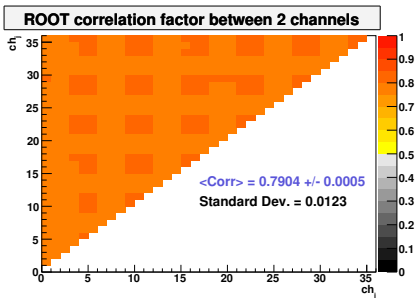

Figure 14: Layer 8, left: stave 2, module 3, before any corrections, right: stave 3, module 2, before any corrections.

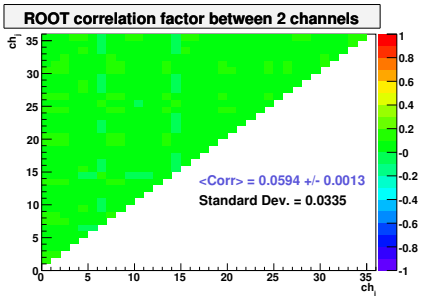

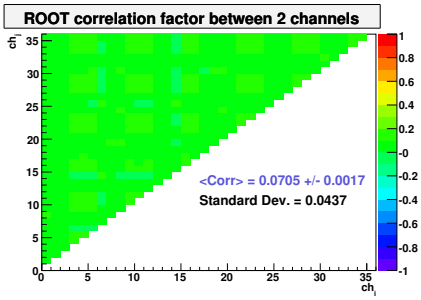

Figure 15: Layer 8, stave 1, left: module 2, after global corrections, right: module 3, after global corrections.

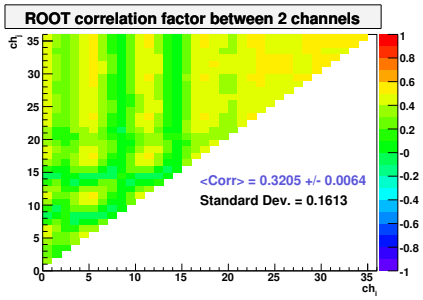

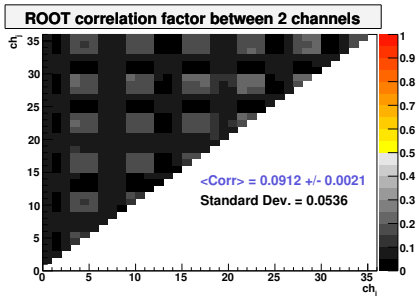

Figure 16: Layer 8, left: stave 2, module 3, after global corrections, right: stave 3, module 2, after all corrections.

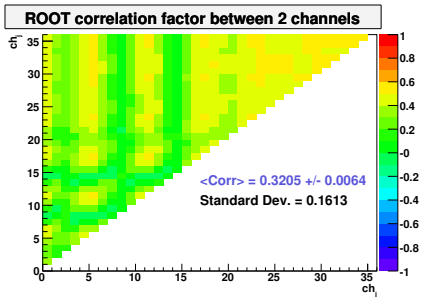

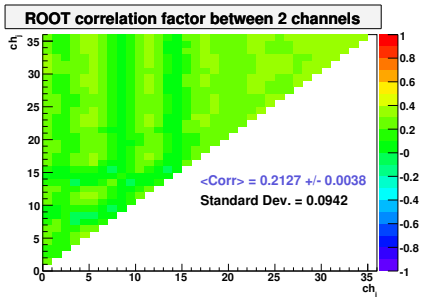

Figure 17: Layer 8, stave 2, module 3, after global corrections, and after global and SIPS corrections.

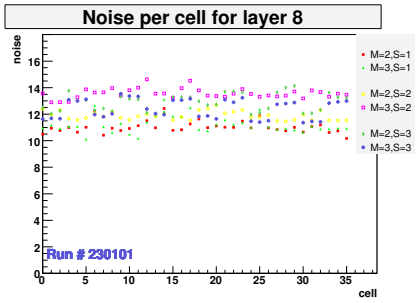

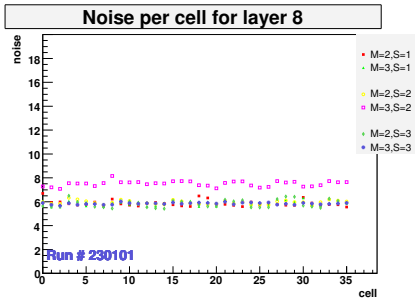

Figure 18: Layer 8, mean noise observed per wafer before any corrections, and after all corrections

- extraction from the pedestal width in beam data

The noise extracted from the convolution of a Gaussian with a Landau function as described in the gain calibration (Sect. 4.1) is shown in Fig. 21. The noise level is narrowly peaked about 7 ADC counts. Since this value is higher than expected the noise has been extracted as well from 11 e^- runs at different energies taken at CERN (8 in August, 3 in October). The reconstruction used includes all currently available corrections for global and signal induced pedestal shifts that are described in the next chapter. Every time a

Figure 19: Layer 8, stave 2, module 3, before any corrections, and after all corrections.

Figure 20: Layer 9, mean noise observed per wafer before any corrections, and after all corrections.

cell has not been hit during an event, the pedestal subtracted and corrected ADC value is added to a histogram. Since the corrections are not to 100% efficient the fitting range of a Gaussian function around 0 has been limited to $(-10, 14)$ ADC. The standard deviation of this Gaussian is then the noise value for this cell. Fig. 22 shows the mean noise value from all the cells for each of the 11 runs. Since the runs are ordered chronologically, this figure represents the evolution of the noise over time during the test beam period at CERN. One can see that the noise is very stable. The small differences can be explained by the varying quality of the corrections. The runs at higher energies thus tend to have a slightly bigger noise due to the small tails of the cells whose noise histograms have been biased by remaining pedestal shifting effects that are known to be dependent on the energy deposit in a wafer and thus the beam energy. The noise for added histograms of all 11 runs is shown in Fig. 23. Here, the noise is narrowly peaked about 6 ADC counts. The small tail for bigger noise is clearly due to the bias of uncorrected events. The mean noise with a perfect correction can thus be expected to be even smaller. The difference of 1 ADC count between the two methods is not completely understood but it may be a fitting artifact from the convolution in the calibration procedure.

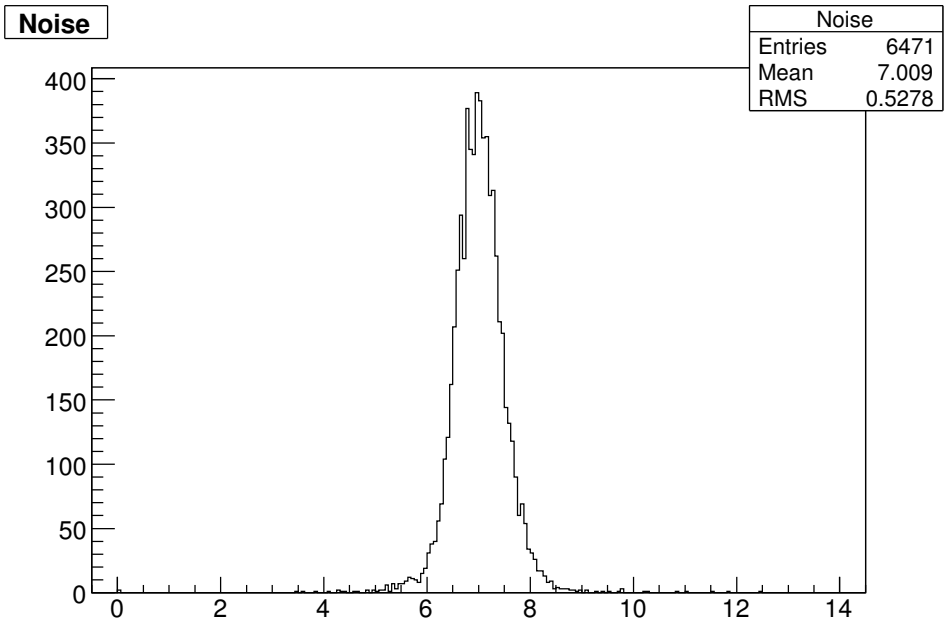

Figure 21: Noise value in ADC counts for the live cells of the ECAL prototype, extracted by a fit on mip signal histograms

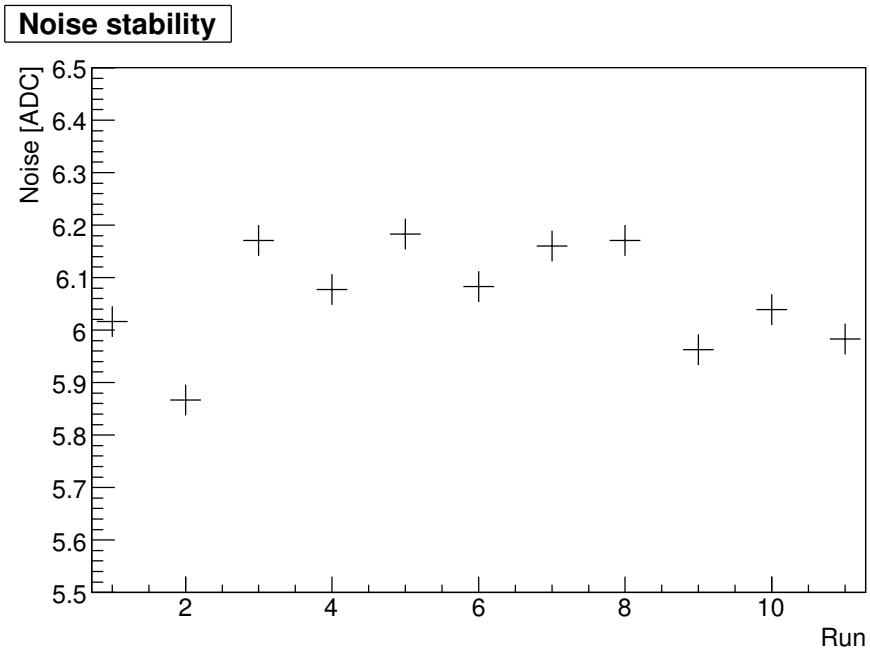

Figure 22: The mean noise value of all live cells in the ECAL for several runs at CERN

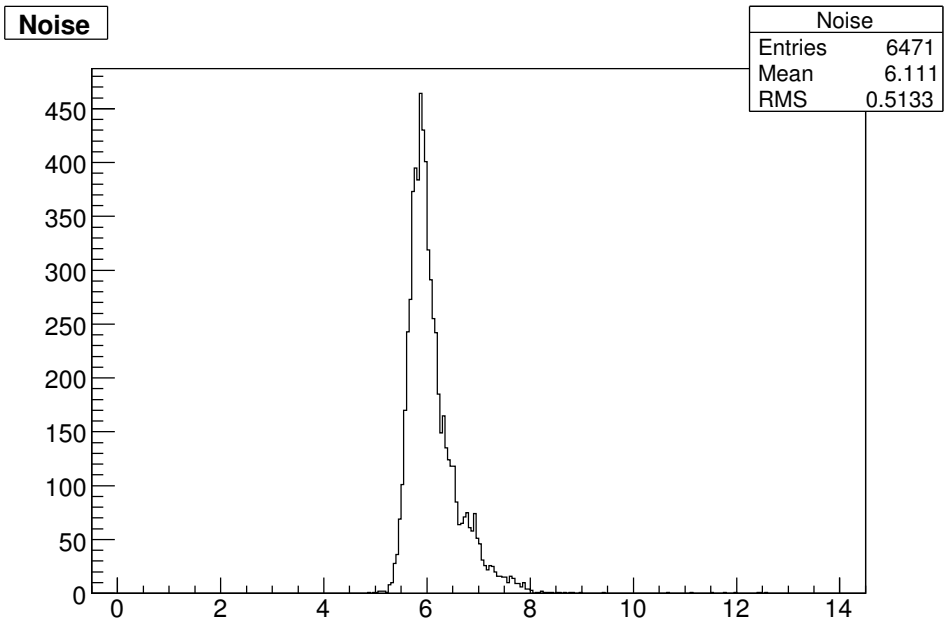

Figure 23: Noise value in ADC counts for the live cells of the ECAL prototype, extracted from the pedestal width in electron runs

5 Monte Carlo simulation

A detailed Geant4 [4,5] based Monte Carlo (MC) simulation of the DESY and CERN test beam setups has been implemented in Mokka [6], version 06-03. The version of GEANT used was 4.8.1.p01.

5.1 The DESY Monte Carlo Simulation

The coordinate system used is right-handed, with the z-axis along the beam line. The back side of the drift chamber closer to the ECAL (**DC1**) defines the $z = 0$ plane. A description of the various detectors is given below.

- **Trigger scintillators (Sc1, Sc2, Sc3)**: plastic scintillators of $200 \times 200 \times 8$ mm^3 ($120 \times 120 \times 8$ mm^3 for Sc3). The hits in the scintillators are simulated as 'calorimeter' hits, so that only one hit per particle traversing the detector is simulated. Hits in each scintillator are written in an output collection in standard LCIO format.
- **Drift chambers (DC1, DC2, DC3, DC4)**: gas chambers of $72 \times 72 \times 88$ mm^3. The gas mixture is 96% Argon and 4% Ethane. The front and back windows are made of mylar and are 20 microns thick. The hits in the drift chambers are simulated as 'tracker' hits. In the real chambers, two sensitive wires give separately the (x, z) and (y, z) positions of the hits generated by the particles traversing the detector. For this reason, the gas volume of the simulated chambers is subdivided in two halves, the first half giving the (x, z) position of the simulated hits, while the second half gives the (y, z) position. The hits are simulated as 'tracker' hits and written out in a single collection containing the hits of all four chambers.
- **Finger counters (Fc1, Fc2)**: plastic scintillators of $100 \times 5 \times 5$ mm^3, placed in T shape along the beam line. The hits in the counters are simulated as 'calorimeter' hits and written in one output collection per counter.
- **ECAL**: the Ecal prototype implementation reproduces in great detail the real prototype. It contains three modules having tungsten absorber thicknesses of 1.4 mm, 2.8 mm and 4.2 mm respectively. Every module is made of three towers, the central and bottom towers being fully equipped with five detector slabs each, while the top tower has only the absorber that is embedded in the carbon fibre structure. There are two silicon planes per detector slab, and they are physically divided into wafers composed of 6×6 cells surrounded by guard-rings. Cell dimensions are 10×10 mm^2 and guard-rings are 1 mm thick, and are divided in three virtual concentric zones. The simulation generates two separate hit collections, one for hits in cells, and the other for hits in guard-rings, which makes possible the study of energy deposits in guard-rings as a function of the distance from the cell border. The five detector slabs of each module are incrementally shifted by 1.3 mm. When using angular incidence, the modules 1 and 3 are shifted in opposite directions, while the central

module (module 2) is not shifted, and the whole prototype is rotated around an axis passing through the centre of module 2. The module shifts have the theoretical values established during the physical module design, but the rotation angle can be specified via a steering command, and can have any value, which allows the simulation of alignment deviations from ideal geometry. A 2 nm thick air layer working like a fake tracker can be added via a steering command in front of the module 1, in order to save particle momentum at the entrance of the Ecal.

The beam simulation is done assuming a monochromatic parallel beam with a Gaussian width, generated 10m upstream of DC1 and passing through the known material.

5.2 The CERN Monte Carlo Simulation

Two separate simulation models have been created for the two different CERN test beam setups. The coordinate system used is left-handed, with the z axis along the beam line. The backside of the drift chamber closer to the ECAL (**DC1**) defines the z=0 plane. A detailed description of the simulated detectors is given below.

- **Cerenkov detector**: $100 \times 100 \times 11000$ mm^3 detector placed 25000 mm upstream of the first scintillator counter. Front and back windows are made of mylar and the gas is helium. Only the material of this detector is simulated, and no sensitive detector is defined.
- **Trigger scintillators (Sc1, Sc2, Sc3, Sc4)**: plastic scintillators of $30 \times 30 \times 15$ mm^3 (Sc1), $100 \times 100 \times 8$ mm^3 (Sc2, Sc4), $200 \times 200 \times 15$ mm^3 (Sc3). The hits are simulated as 'calorimeter' hits and written in one output collection per scintillator.
- **Drift chambers (DC1, DC2, DC3)**: gas chambers of $100 \times 100 \times 44$ mm^3. The gas mixture is 50% Argon and 50% CO_2. The front and back windows are made of kapton and are 20 microns thick. The hits in the drift chambers are simulated as 'tracker' hits and written out in a single collection containing the hits of all four chambers.
- **ECAL**: the Ecal prototype is the same as that in the DESY setup. For the October setup, only normal incidence should be used, as in the real experiment, due to the small distance between Ecal and Hcal.
- **HCAL**: in the August setup, the detector is made of 35 layers of $900 \times 900 \times 30$ mm^3. Each layer is made of an iron absorber and a scintillating material and is sub-divided into 90×90 cells of 10×10 mm^2. These cells are then mapped onto the real 30×30 mm^2, 60×60 mm^2,120×120 mm^2 tiles as part of the analysis procedure. In the October setup, the detector is made of only 30 layers, having the same characteristics described above.

- **Muon counters (Mc1, Mc2)**: plastic scintillators with dimensions $1000 \times 1000 \times 9.5$ mm^3. Hits in the scintillators are simulated as 'calorimeter' hits and written in one output collection per detector. In the October setup, only one muon chamber (Mc1) is present on the beam line.

- **Tail Catcher**: in the August setup the detector is made of 16 layers (absorber+air gap+readout module), not fully instrumented. The absorbers (1168×1168 mm^2) have 2 different thicknesses: 19 mm (layer 1 to 8) and 101 mm (layer 9 to 16). The readout modules have 9.5 mm thickness. The air gaps are 22 mm thick. All absorbers are in place, but there are only 8 readout modules: layer 1, 4, 7, 10 (vertical strips) and layer 2, 5, 8, 11 (horizontal strips). Layers 3, 6, 9, 12-16 have no readout modules and a 32 mm-thick air gap. In the October setup all the layers are fully instrumented. The absorbers have 2 different thicknesses: 19 mm (layer 1 to 8) and 102 mm (layer 9 to 16). The readout modules have 9.5 mm thickness. The air gaps are 22 mm thick.

The beam simulation is done assuming a monochromatic parallel beam with a Gaussian width, generated 50m upstream of DC1 and passing through the known material.

5.3 Reconstruction of MC events

Where required, the generated signals from the ECAL and drift chambers may be digitised during the reconstruction phase of the MC production.

In the ECAL, the digitisation step is done using a processor in Marlin. The conversion of the simulated energy to ADC counts is done using calibration factors obtained from real data, which are assumed to be constant and are calculated per cell. The noise is added by calculating a random value per cell and per event, based on the average noise observed in data. A flat distribution of pedestal of 0 ± 0.5 ADC counts is taken and, when cells have signal, the noise is added to it. In case of no signal, new cells are created using only the value for the noise. If a given cell was not working in the real data because of problems in the corresponding PCB, a flag is defined and the cell is declared dead in the MC as well. Cells are also declared dead in case the pedestal of the corresponding cell in real data is too high or some other errors are observed for that particular cell in the real data.

After the digitisation, the hits are reconstructed in the same way as for real data: the calibration is performed and the reconstructed data are saved as calorimeter hits. The position of the hits is calculated from a mapping of the cells in the ECAL.

For the drift chambers, the digitisation is done using the TBTrackDigitizer Marlin processor. For each chamber, each hit is randomly kept or rejected according to an efficiency value and, for those retained, the hit position is randomly smeared by a Gaussian with a width set to the measured chamber intrinsic resolution. The resulting positions, in x or y depending on the chamber, are then converted to a TDC hits using realistic chamber constants. In addition, noise hits are generated randomly over the whole chamber fiducial

volume and are also converted to TDC hits. The noise hit rate is chosen to approximately match that seen in the data. The digitised hits are then written out to different hit collections, where the TDC value of the hit and the ID of the drift chamber where the hit occurred are stored. Following this, the TBTrackProducer processor reconstructs tracks from these TDC hits as described in Sec. 7.4.

6 Electron Selection

The triggering of the test beam setups was explained in Sect. 3. Further cuts were then applied in order to select samples of single beam electrons for further study. These cuts are intentionally loose at this stage; for specialised studies, more stringent selections may be applied, and will be discussed below as appropriate.

The most important cut is on the total energy in the ECAL. In order to remove most of the noise signals, a threshold cut of 0.6 MIP is imposed on the energies of individual cells (around five times the average pedestal width). The total energy recorded in the ECAL, E_{raw}, is then calculated, with the three stacks weighted in proportion to the tungsten thickness, i.e. in the ratios 1:2:3. In Fig. 24 we show the distributions of this energy, in MIPS, for two typical runs, one from DESY at 3 GeV, and one from CERN at 20 GeV. The peaks around 750 MIP and 5000 MIP respectively correspond to single beam electrons. In the case of the DESY beam, a clear peak corresponding to two beam electrons is seen at around 1500 MIP. In addition, at DESY, a sizeable low energy contribution is seen, which appears to be caused by beam halo of low energy electrons and photons, spread rather uniformly across the calorimeter. At CERN, there is a peak at about 50 MIPs corresponding to muon or pion contribution in the beam. The cut applied is:

$$125 \times E_{\mathrm{beam}} < E_{\mathrm{raw}} \,/\mathrm{MIP} < 375 \times E_{\mathrm{beam}} \quad .$$

The cuts are indicated in Fig. 24, and can be seen to select the desired peak, and to eliminate most of the background.

Further cuts are applied to some of the samples.

- For some of the CERN runs, such as that shown in Fig. 24, there was a significant pion content. This can be reduced by using the threshold Čerenkov counter in the beam. The shaded region in Fig. 24 indicates the effect of demanding a trigger signal from the Čerenkov counter – it greatly reduces the pion contamination, whilst having little effect on the electron peak.
- For some studies using the DESY beam, additional cuts on the shower barycentre were imposed, to ensure that the event lay in the region expected from the beam profile; the low energy beam halo being distributed more or less uniformly across the calorimeter.

The effect of these two additional cuts is indicated by the shaded regions in Fig. 24.

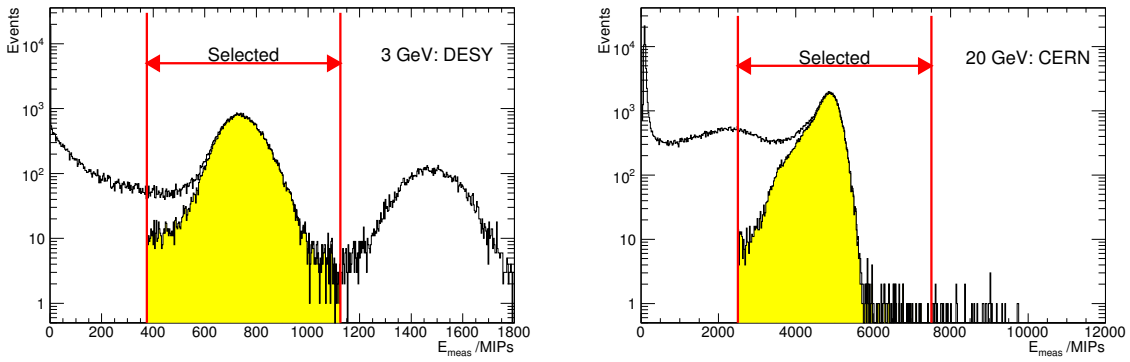

Figure 24: *Distribution of total ECAL hit energies for a 3 GeV* e^- *beam at DESY (left) and for 20 GeV at CERN (right). The cuts used to isolate the main electron signal are indicated. The shaded area in the 3 GeV plot shows the effect of additional cuts on the shower barycentre intended to reduce out-of-beam halo. The shaded area in the 20 GeV plot shows the effect of demanding a signal from the Čerenkov counter in reducing the pion contribution.*

7 Performance Studies

7.1 Energy Response, Linearity and Resolution

As explained above, after calibration, the ECAL data consist of hit energies in the cells of the calorimeter in units of MIPs. In order to remove most of the noise signals, a threshold cut of 0.6 MIP is imposed (around five times the average pedestal width).

In the Monte Carlo, the ionization energy deposited in each cell is accumulated. For simple comparisons with data, a single calibration is used in order to convert this to MIPs using 0.147 MeV≡1 MIP, and Gaussian noise with r.m.s.=0.12 MIP is added. For more sophisticated comparisons, the full digitisation procedure outlined in Sect. 5.3 may be used, which takes account of cell-to-cell variations in the gain and noise.

In Fig 25 we show the distribution of hit energies when the ECAL was exposed to a 12 GeV π^- beam. For this comparison, the total energy in the ECAL was required to lie between 20 and 150 MIPs, to remove events in which any significant hadronic shower development had occurred; the hits are therefore predominantly caused by non-interacting pions, i.e. MIPs. A strong peak at 1 MIP is seen, largely corresponding to non-showering π^-; the position and width of the peak are quite well modelled by the very naïve simulation.

In Fig 26 we show the corresponding distribution when the ECAL was exposed to a 30 GeV e^- beam. The data are shown twice; first on a linear scale to emphasise the region around the 1 MIP peak, and on a logarithmic scale to emphasise the tail of high energy hits. The tail of the distribution, corresponding to cells in the core of the showers with energies up to $\sim$ 350 MIPs, is very well modelled. The region below and up to the 1 MIP peak shows some discrepancies, which are the subject of current investigation.

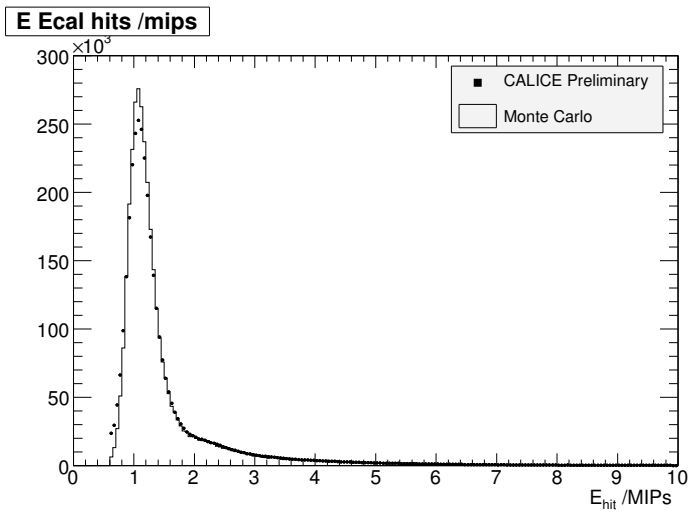

Figure 25: *Distribution of ECAL hit energies for a 12 GeV π^- beam. Data are shown as points; simulation as the open histogram.*

These discrepancies have little effect on the total energy, though they do influence the number of cells hit. For this reason, the present studies emphasise the energy deposition in electromagnetic showers showers and its distribution.

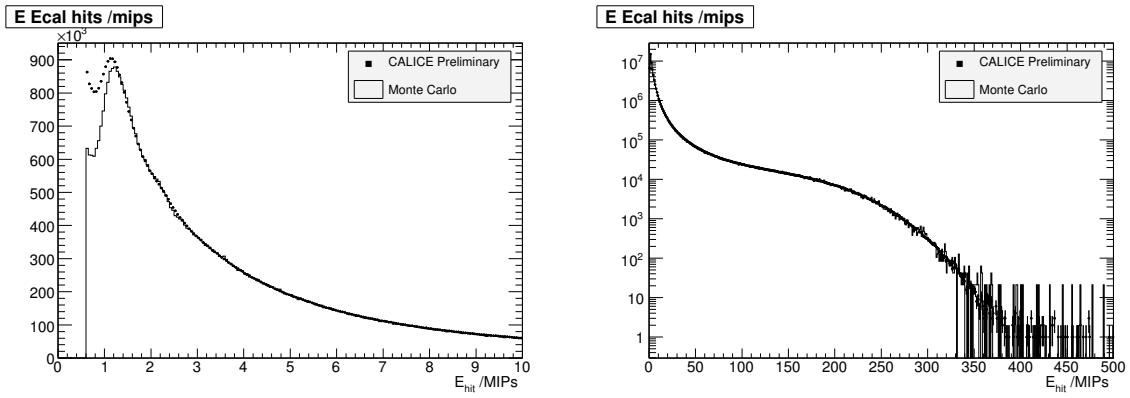

Figure 26: *Distribution of ECAL hit energies for a 30 GeV e^- beam. Data are shown as points; simulation as the open histogram. The same data are shown on both linear and logarithmic scales.*

The total response of the calorimeter may be computed by summing the hit energies in the three sections of the detector: E_1 being the energy in the first ten layers, E_2 in the next ten, and E_3 in the rear ten. The total response is then given by

$$E_{\rm tot} = (\alpha_1 E_1 + \alpha_2 E_2 + \alpha_3 E_3)/\beta \ .$$

The naive choice for the weights $(\alpha_1, \alpha_2, \alpha_3)$ is $(1., 2., 3.)$, reflecting the relative thicknesses of the tungsten layers in each of the sections of the calorimeter, and hence the relative sampling fractions. The normalisation β is taken to be 250 MIP/GeV; this parameter has

not been optimised, so the overall scale of corrected energy is somewhat arbitrary. For comparison, we also show some results using an optimised set of weights $(\alpha_1, \alpha_2, \alpha_3) = (1.1, 2., 2.7)$, which prove to give a slightly improved performance in terms of resolution and linearity.

The inter-wafer gaps of 2 mm, caused by the guard rings, have an influence on the response when showers traverse these regions of the calorimeter. This is illustrated in Fig 27 for 30 GeV e^- impinging on the calorimeter at normal incidence, where the mean energy is plotted as a function of the shower centre-of-gravity or barycentre:

$$(\bar{x}, \bar{y}) = \sum_i (E_i x_i, E_i y_i) / \sum_i E_i$$

(where the sums run over all hit cells in the calorimeter). Dips in response at $\bar{y} \sim -9$ mm and $\bar{x} \sim -26$ and $+36$ mm are clearly visible, and account for the asymmetric tail on the low side of the distribution of total energy. As shown in Fig 27, this asymmetry in the peak is reasonably well modelled by the simulation. Possible ways of correcting for these gaps are discussed in Sect. 7.1.1 below.

The beam profile, and therefore the fraction of beam particles traversing the regions of the inter-wafer gaps, depends on the beam energy. Therefore, in order to study the response of the calorimeter as a function of energy with a minimum of bias, we apply a cut on the shower centre-of-gravity so as to remove showers close to the gaps. The cut imposed is:

$$-16 < \bar{x} < +26 \text{ mm} \quad ; \quad 1 < \bar{y} < +41 \text{ mm}$$

thereby selecting particles impinging on the calorimeter near the middle of the upper central wafer. The total energy is then histogrammed for the selected events, and the peak is fitted by a Gaussian function in the range $[-\sigma : +2\sigma]$. An asymmetric range is chosen in order to reduce sensitivity to pion background, to radiative effects upstream of the calorimeter, and to any residual influence of the inter-wafer gaps. The position of the peak is taken to be the mean energy response. A typical fit, for electrons at 30 GeV, is shown in Fig.28. The fits are of good statistical quality.

In Fig. 29 we show the reconstructed energy, plotted against the beam energy, for e^- data recorded at CERN and DESY in the range 1–45 GeV. The results are shown for two choices of the weights $(\alpha_1, \alpha_2, \alpha_3)$. On this scale, excellent linearity is observed. To test this more critically, in Fig. 30 we show the reconstructed energy, divided by the beam energy, for e^- data recorded at CERN in the range 6–45 GeV. The results are shown for two choices of the weights $(\alpha_1, \alpha_2, \alpha_3)$. We observe that the linearity is somewhat better for the optimised choice $(\alpha_1, \alpha_2, \alpha_3) = (1.1, 2, 2.7)$. The slight overall shift could be corrected by a different choice for the overall normalisation β, of course. The values are generally consistent with a common mean to within approximately $\pm 1\%$. In Fig. 31 we show the analogous plot for e^- data recorded at DESY in the range 1–6 GeV. The results at DESY are not directly comparable with those from CERN because six of the layers of silicon sensors were absent. No correction for this has yet been made. The average effect is a loss of energy which increases from $\sim 1 - 3\%$ as the electron energy goes from $1 - 6$ GeV, as discussed in Sect. 7.2 below.

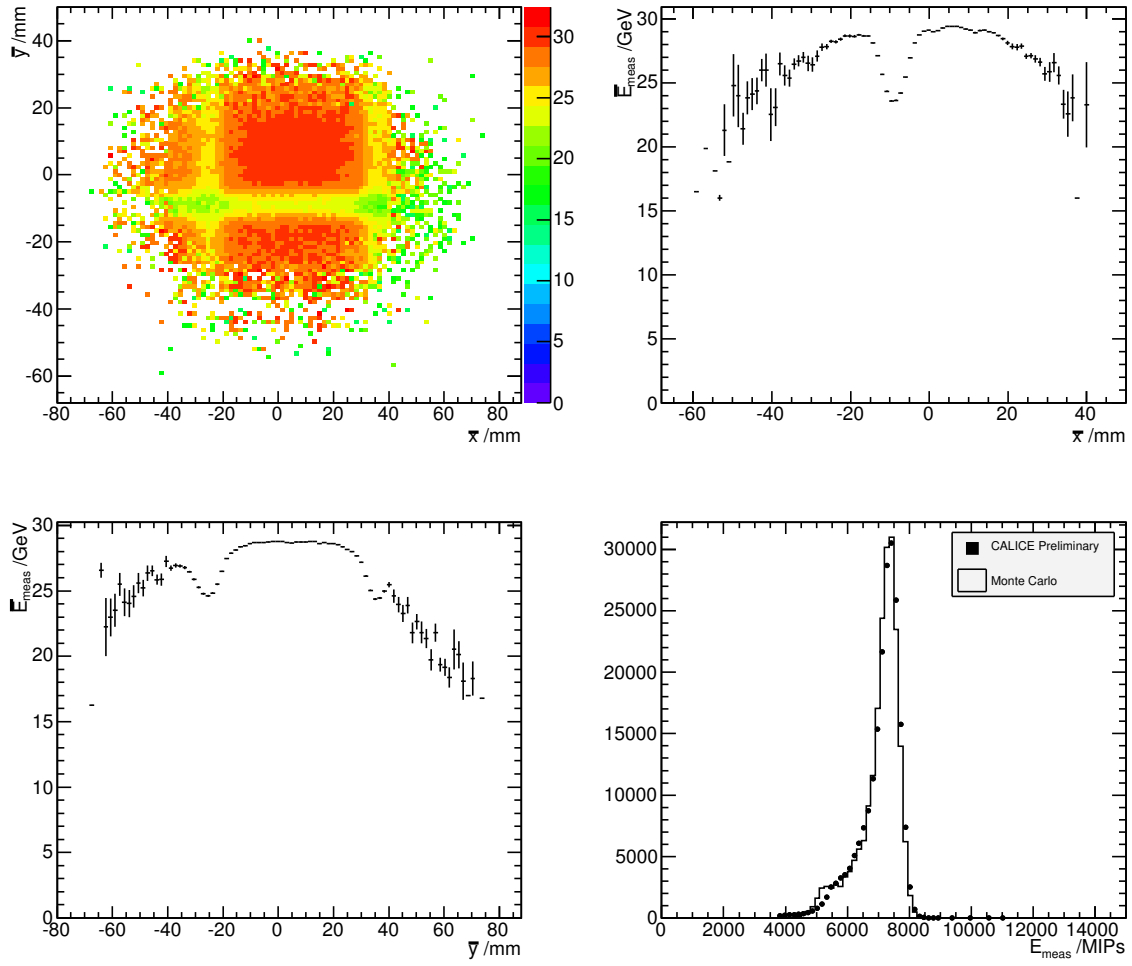

Figure 27: *Mean total ECAL energy for a 30 GeV* e^- *beam. In the upper left plot the mean energy is plotted as a function of the shower centre-of-gravity* $(\bar{x}, \bar{y})$ *(in mm). In the upper right and lower left plots the mean energy is plotted as a function of* $\bar{y}$ *and* $\bar{x}$*, and in the lower right the distribution of energy in data (points) is compared with Monte Carlo (open histogram).*

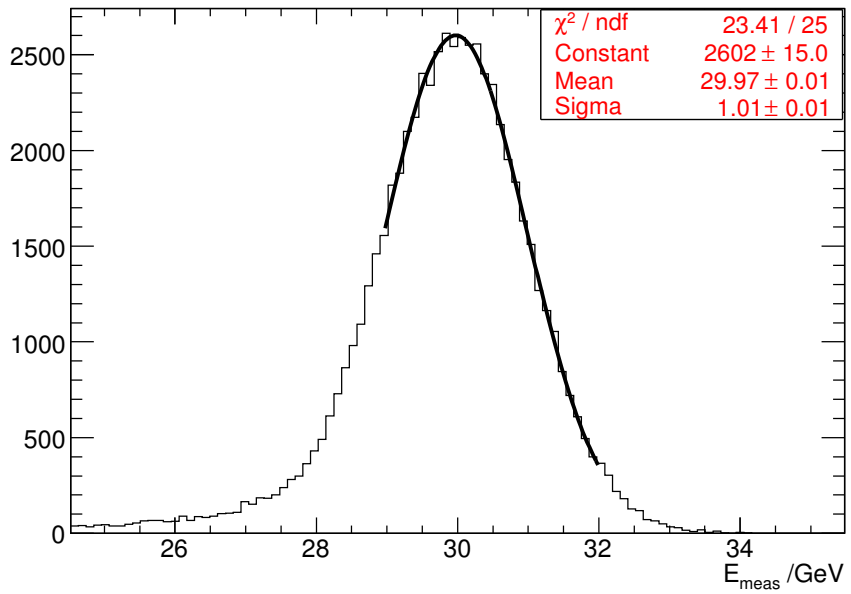

Figure 28: *An example of a Gaussian fit to the measured energy, for data recorded using an electron beam at 30 GeV. Such fits are used to estimate the mean response and energy resolution of the calorimeter.*

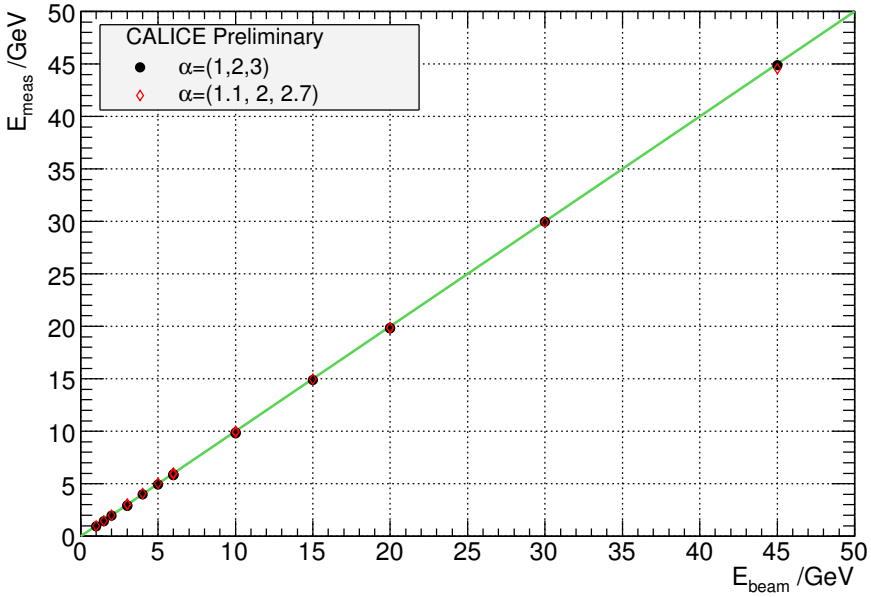

Figure 29: *Energy response of the ECAL, roughly but not optimally calibrated to the beam energy, plotted as a function of beam energy. The plot relates to electron beam data from DESY and CERN taken at normal incidence, with energies 1–45 GeV. Two possible weightings of the different calorimeter stacks are compared. The line represents* $E_{\mathrm{meas}} = E_{\mathrm{beam}}$.

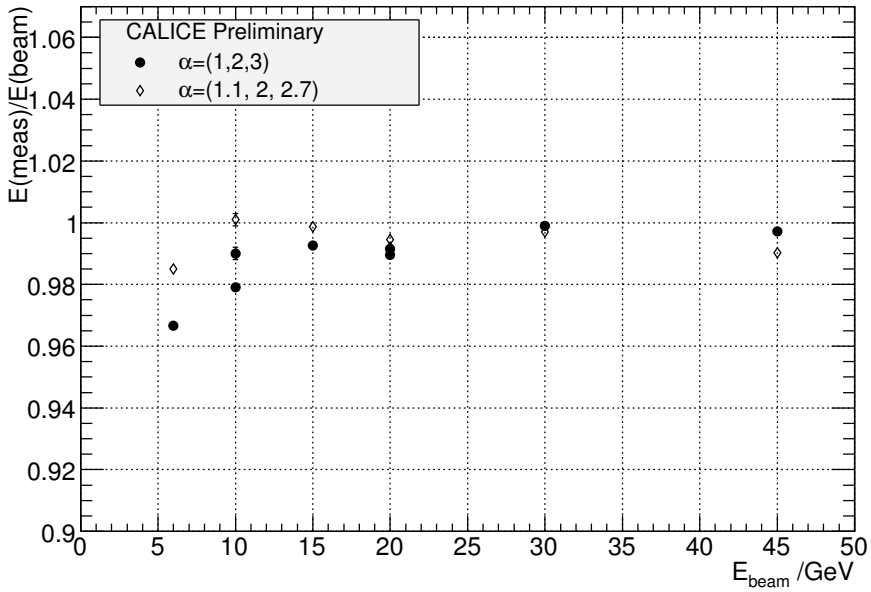

Figure 30: *Energy response of the ECAL, roughly but not optimally calibrated to the beam energy, divided by beam energy, plotted as a function of beam energy. The plot relates to electron beam data from CERN taken at normal incidence, with energies 6–45 GeV. Two possible weightings of the different calorimeter stacks are compared.*

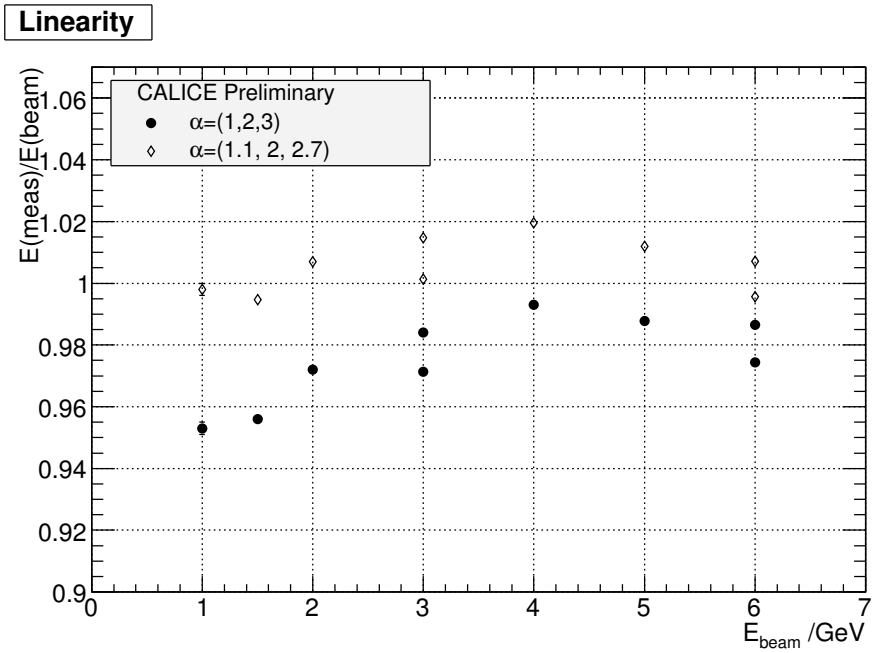

Figure 31: *Energy response of the ECAL, roughly but not optimally calibrated to the beam energy, divided by beam energy, plotted as a function of beam energy. The plot relates to electron beam data from DESY taken at normal incidence, with energies 1–6 GeV. Two possible weightings of the different calorimeter stacks are compared.*

In Fig. 32 we show the fractional energy resolution for e^- data recorded at CERN and DESY in the range 1–45 GeV. The observed resolution is compatible with an approximately linear dependence on $1/\sqrt{E}$ as naïvely expected from the statistical sampling of the shower energy. Using the naïve choice of weights, $(\alpha_1, \alpha_2, \alpha_3) = (1, 2, 3)$, the resolution may be parametrised by a quadrature sum of statistical and constant terms

$$\Delta E/E = \left(17.67 \pm 0.07/\sqrt{E(\mathrm{GeV})} \oplus 1.07 \pm 0.08\right) \% \quad ,$$

while using the alternative choice of weights, $(\alpha_1, \alpha_2, \alpha_3) = (1.1, 2, 2.7)$ we obtain

$$\Delta E/E = \left(17.13 \pm 0.07/\sqrt{E(\mathrm{GeV})} \oplus 0.54 \pm 0.15\right) \% \quad .$$

An alternative, and less well motivated, parametrisation in terms of of a simple sum of a statistical and a constant resolution term happens to fit the data with a slightly better χ^2, yielding

$$\Delta E/E = \left(17.37 \pm 0.10/\sqrt{E(\mathrm{GeV})} + 0.24 \pm 0.03\right) \% \quad ,$$

for $(\alpha_1, \alpha_2, \alpha_3) = (1, 2, 3)$ and

$$\Delta E/E = \left(16.99 \pm 0.10/\sqrt{E(\mathrm{GeV})} + 0.10 \pm 0.03\right) \%$$

when using the alternative choice of weights, $(\alpha_1, \alpha_2, \alpha_3) = (1.1, 2, 2.7)$. In either case, the resolution is improved by a factor of typically $\sim 0.95 - 0.97$ by the optimised weights. The naïve weighting therefore appears to be not far from optimal. Also in Fig. 32 we show the fractional energy resolution predicted by Monte Carlo, analysed in the same way as data, for the choice $(\alpha_1, \alpha_2, \alpha_3) = (1, 2, 3)$. The agreement with data is quite good, with the resolution seen in data typically worse than predicted by a factor ~ 1.02.

7.1.1 Correction of gaps

As discussed in the previous section, the energy loss for events within the inter-wafer gaps is important: ~ 14 % in x, ~ 19 % in y right in the centre of the gaps. In order to account for this collection efficiency loss and to make the calorimeter response more uniform, a simple method correcting the shower energy as function of the position of the global barycentre (centre-of-gravity) $(\bar{x}, \bar{y})$ was investigated.

To minimise the impact of the shower energy on the corrections, they were defined using a combined sample of 10, 15 and 20 GeV electrons, equally populated. Figure 33 shows the calorimeter response (normalised to the beam energy) for this sample as function of $\bar{x}$ and $\bar{y}$ respectively.

The distributions around the inter-wafer gap positions were fitted with Gaussians, independently in $\bar{x}$ and $\bar{y}$:

$$\left(1 - a_x \exp \frac{-(x_b - x_{gap})^2}{2\sigma_x^2}\right) \times \left(1 - a_y \exp \frac{-(y_b - y_{gap})^2}{2\sigma_y^2}\right)$$

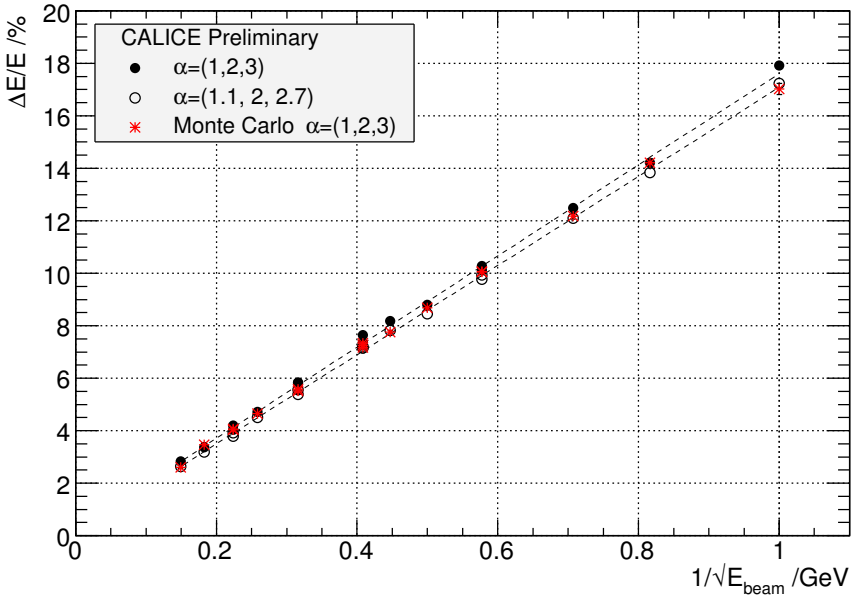

Figure 32: *Fractional energy resolution of the ECAL, plotted as a function of* $1/\sqrt{E}$*. The plot relates to electron beam data from DESY and CERN taken at normal incidence, with energies 1-45 GeV. Two possible weightings of the different calorimeter stacks are compared. A Monte Carlo simulation is also shown.*

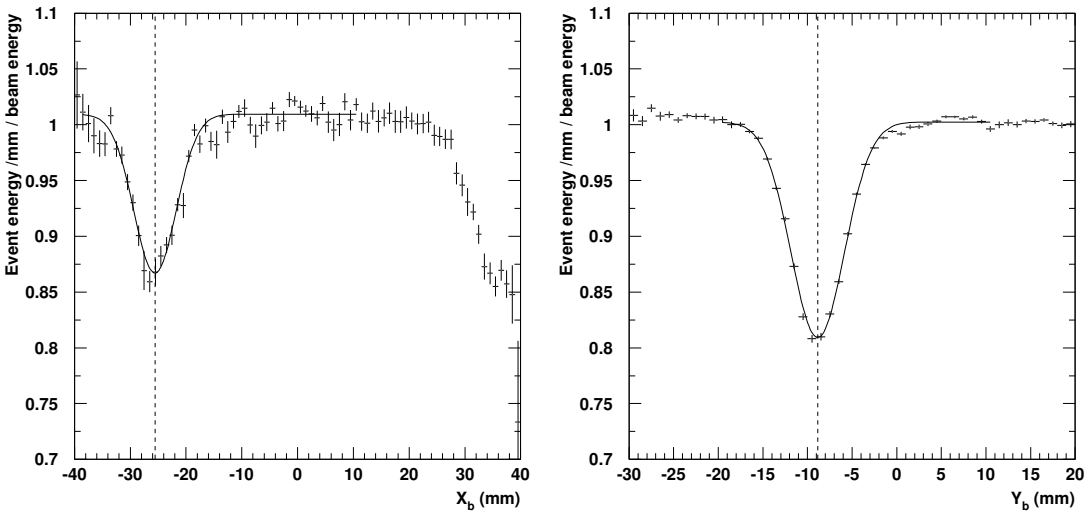

Figure 33: *Normalised calorimeter response as function of the shower barycentre coordinates* $\bar{x}$ *and* $\bar{y}$ *(in mm), for a combined sample of 10, 15 and 20 GeV electrons. To characterise the* x *(*y*) response, the events were requested to be outside the inter-wafer gap in* y *(*x*), leading to an important difference in the number of events for the two distributions, since the* y *gap is approximately centred on the beam.*

The second x inter-wafer gap (at ∼34 mm) is difficult to characterise since it is insufficiently covered by the beam. Since its effect should be identical to the first (∼-26 mm) gap, only the last was fitted and the obtained correction was applied to both gaps. The results of the fits are given in table 5. Note that the gap in x is shallower but wider than that in y, owing to the staggering of the gaps in x.

	x_{gap}, y_{gap}	σ_x, σ_y	a_x, a_y
x direction	-25.56	3.8	0.14
y direction	-8.8	3.01	0.19

Table 5: Gaussian fits of the inter-wafer gaps.

The corrections are not applied if the calculated barycentre coordinates of the shower are more than 4σ away from the fitted gap positions. They work well on average and the calorimeter response is flattened, as illustrated in figure 34.

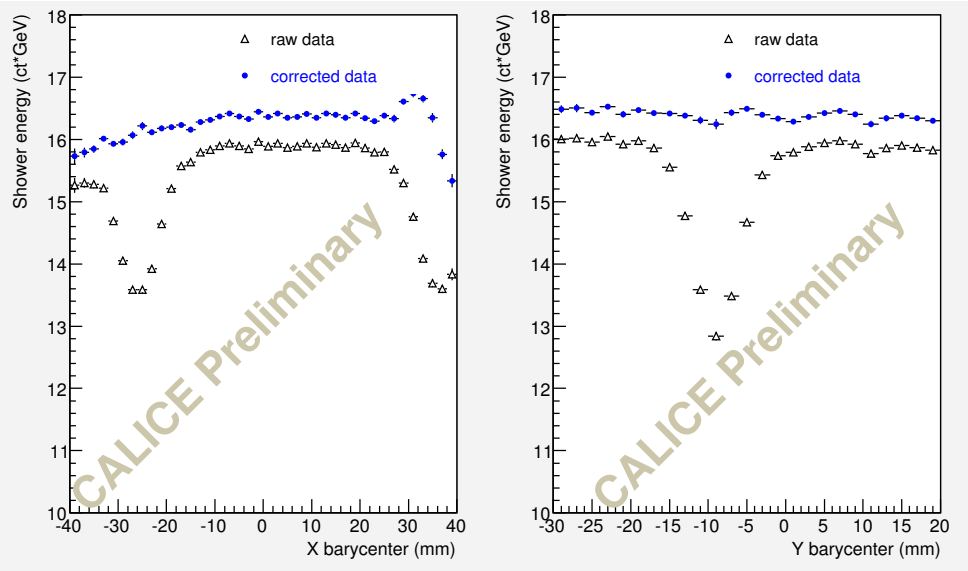

Figure 34: Calorimeter response as function of the shower barycentre coordinates ($\bar{x}$, $\bar{y}$), for 15 GeV electrons, before (black triangles) and after the corrections (blue circles) were applied on the measured energy.

Figure 35 shows the important reduction in the low energy tail of the energy distribution for 15 GeV electrons. On the same figure, the red histogram represents the energy distribution for the events outside the gaps, upscaled by a factor 3, for an easier comparison. The resolution loss when going from the clean events to all the events, with corrections applied on the energy, is of the order of 10%.

The corrections apply successfully to all the energies considered (6 to 45 GeV), as illustrated in figure 36.

A gap correction method working on a layer-by-layer basis is also under development. It is based on the assumption that the signal loss is approximately proportional to the

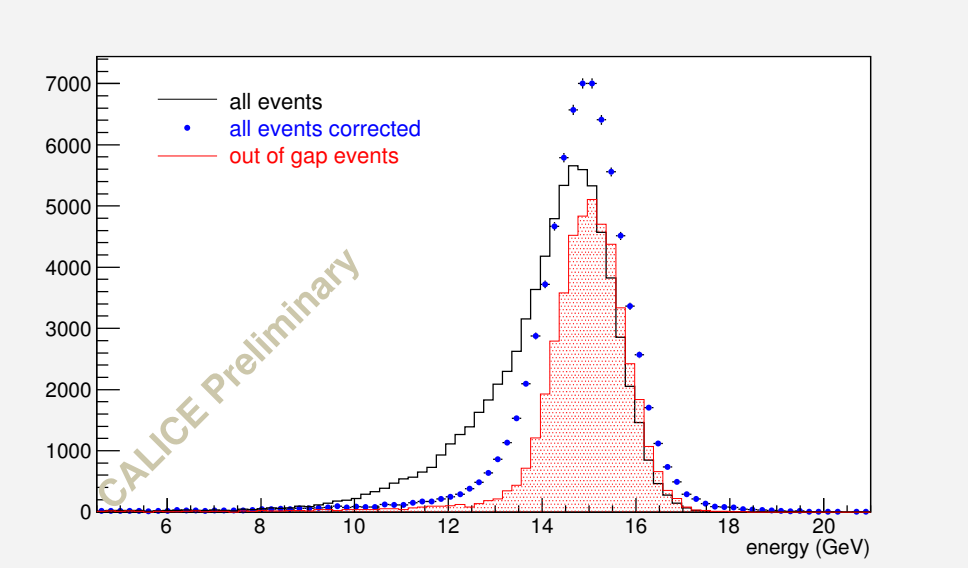

Figure 35: Energy distribution for 15 GeV electrons in case of : events outside the inter-wafer gaps (red histogram), all events without corrections (black histogram) and all events with corrections (blue circles). The red histogram was upscaled by a factor 3 for easier comparison.

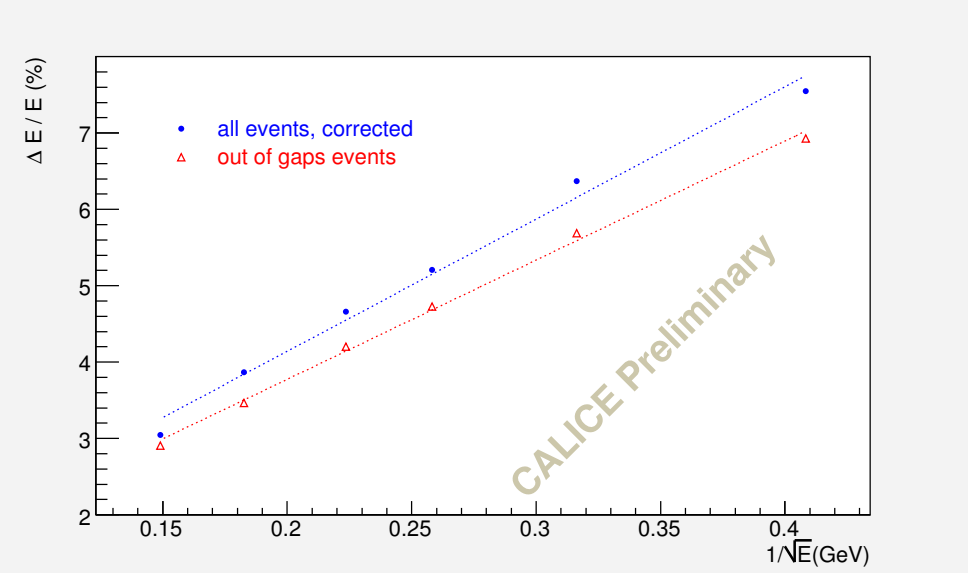

Figure 36: $\frac{\Delta E}{E}$ as function of $\frac{1}{\sqrt{E}}$ for events outside the inter-wafer gaps (red triangles) and for all events with corrections applied on the shower energy as function of the shower barycentre position (blue circles). It should be noted that the beam profile changes with the beam energy leading to different relative contributions of the events within the inter-wafer gaps to the overall distributions.

insensitive area of the detector caused by interwafer gaps. By estimating the fraction of the shower that lies in the gap one can subsequently recover the signal lost. The method assumes the knowledge of the position of the shower with respect to the gap and the transverse size of the shower at each layer. The former is provided by the tracking system, the latter as a first approach is approximated by the energy weighted RMS of position of the shower hits in each layer. Taking these into account the relative area and thus the signal that would be readout if there were no gaps can be estimated. Applying this procedure for each layer of the detector and for each event we can compensate for the signal loss due to insensitive areas. One should note that the method does not require the prior knowledge of the incident energy and so it can be applied not only to test beam data but also to the full scale experiment.

An example of application to test beam data is shown in Figure 37. The drop of signal when the electron beam is entering the calorimeter around the edge between two wafers is clearly seen at the plots of the left column. The right column displays the same set of data after the correction method is applied on each event. The signal loss is recovered with high efficiency.

7.1.2 Dependence on angle

In addition to the data recorded with the beam at normal incidence, described above, the electromagnetic calorimeter prototype was also tested with electron beams at different angles: 10, 20, 30 and 45 degrees at DESY, and only 20, 30 and 45 degrees at CERN. Actually, the prototype was rotated around the vertical axis (y) and the three stacks (each composed of 10 detection layers) were translated laterally to have the electromagnetic showers inside the active part of the calorimeter. The inter-wafer gaps were not aligned, this misalignment increasing as a function of the angle value. Such a detection system simulates a more realistic configuration of the final version of the detector.

The correction for effects due to the inter-wafer gaps becomes in that case much more complicated because the correction depends on the position and the size of the showers as a function of layer. Our first and preliminary approach to restore the energy lost in the wafer guard rings is the following:

1. virtual cells are added in the gap,
2. between two cells there is only one virtual cell,
3. the energy in the virtual cells is the sum of the energies deposited in the two closest cells multiplied by a constant determined after an optimisation study. It leads to the formula:

$$E_{virtual\ cell} = k \times (E_{i-1} + E_{i+1})$$

where k=0.05 instead of k$\simeq$0.1 deduced directly from the surface ratio.

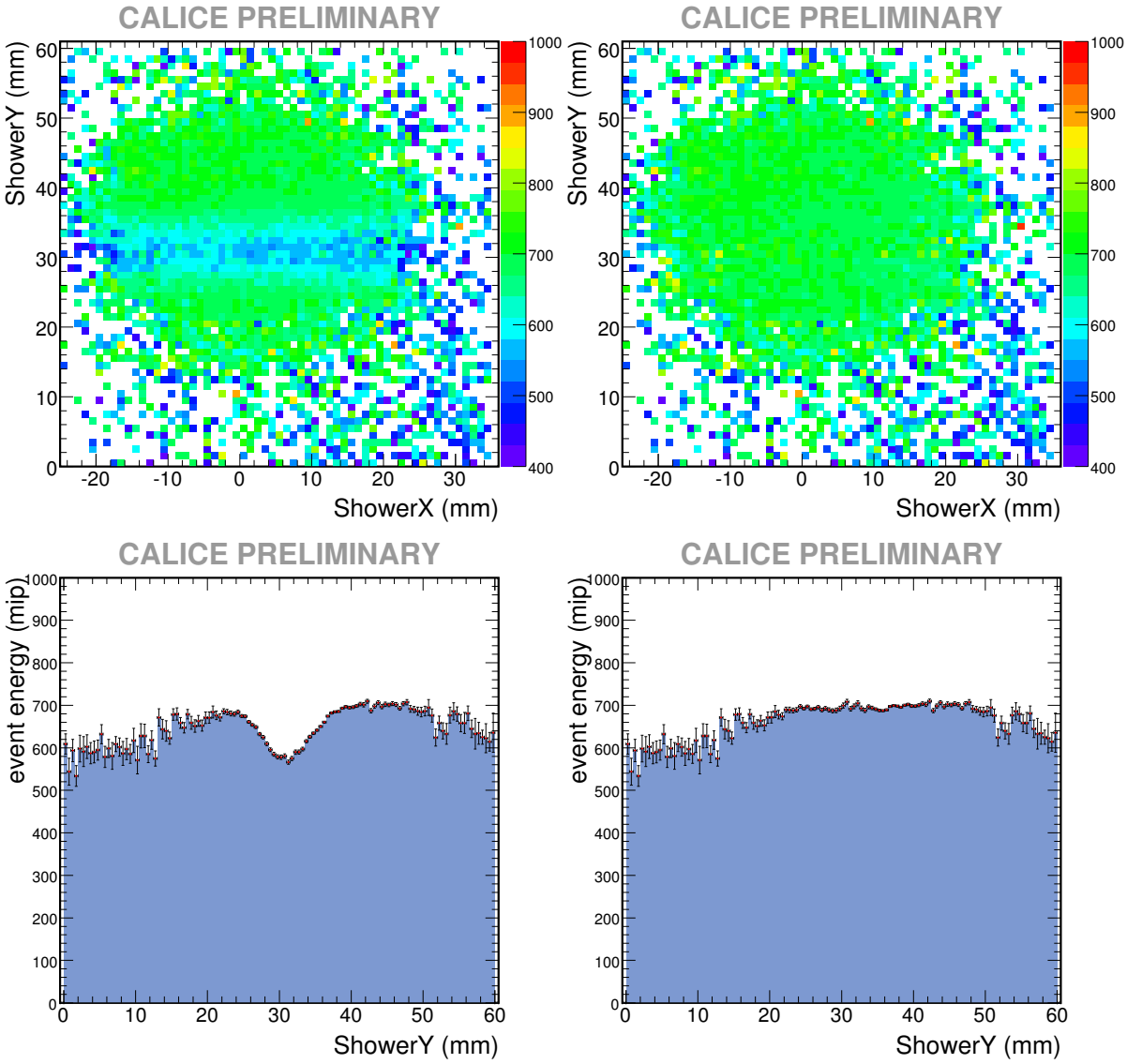

Figure 37: *Detector response to 3 GeV e^-, expressed in color coded scale mip units, versus the shower barycenter and projection along the vertical direction before (left column) and after (right column) the gap correction method is applied.*

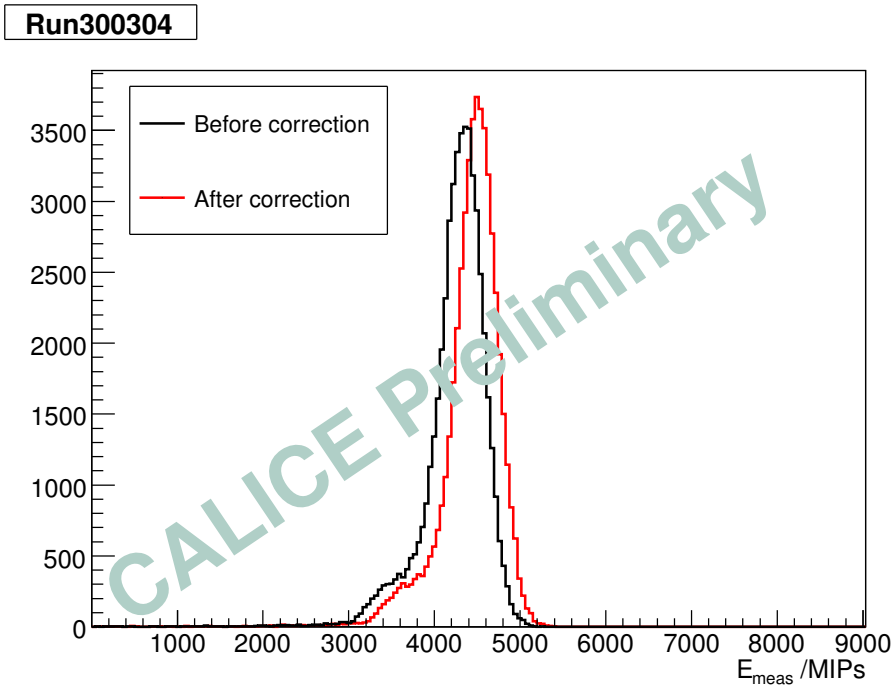

Figure 38: *Energy distributions, with and without inter-wafer gap correction, for 20 GeV electrons at 45º.*

This correction was applied for each layer and event by event.

Figure 38 shows the energy distributions, with and without this inter-wafer gap correction, for 20 GeV electrons at 45°. One can observe that the corrected distribution is shifted towards higher energies and the new peak is slightly higher implying a better energy resolution.

Figure 39 shows a compilation of our results after the inter-wafer gap correction. Note that the measurements below 6 GeV were done at DESY where the prototype was only equipped with 24 detection layers.

7.2 Longitudinal shower development

The study of the longitudinal profile of the electromagnetic shower applies the same minimal event selection criteria as used previously. This requires events to have a total energy measured in the ECAL within 50% of the nominal beam energy, and all to have a minimum energy equivalent to 0.6 MIPs. Several data samples taken at CERN have a mixed e^-/π beam. Therefore a cut on the Čerenkov trigger is applied for those runs to suppress the π events in the data samples. To reduce the contribution from events in which significant showering starts before the beam is incident upon the first layer of the ECAL, potentially biasing the longitudinal profile, one additional selection criteria is applied to the events used. This consists of calculating the mean position and variance

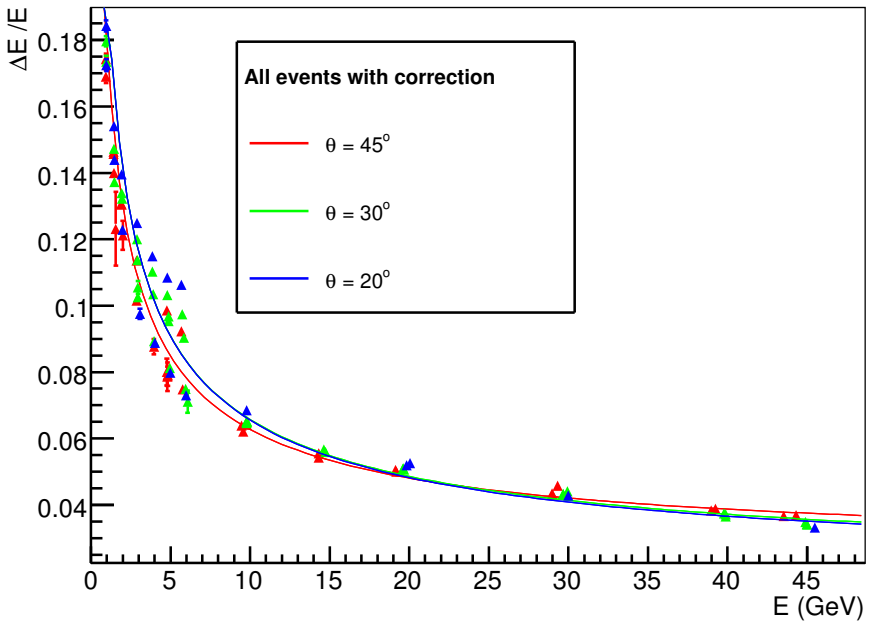

Figure 39: Energy resolution after the inter-wafer gap correction.

from the measured x and y co-ordinates of all ECAL hits in the most upstream layer, and using these to form a χ^2 from the x and y hits in this layer of the detector. Events in which this $\chi^2 > 20$ are rejected.

In this analysis, as no correction is made for the reduced efficiency in the region between each wafer, the measured mean transverse position of all hits above threshold is required to be within 20mm of the nominal centre of a wafer in both x and y. Similarly, the energy attributed to each layer is weighted according to the nominal thickness of tungsten absorber immediately upstream, therefore layers 1-10:11-20:21-30 have relative weights of 1:2:3.

An example of the measured energy distribution as a function of calorimeter depth in data recorded at CERN data with an e^- beam energy of 20 GeV is given in Figure 40, together with a parametrisation of the profile used. The fitted function, is given by $\gamma(t) = c\,t^{\alpha}\exp(-\beta t)$, where t is the calorimeter depth, c is an overall normalisation, α is the exponent of the calorimeter depth, t, and β is a constant which determines the rate of exponential decay as a function of calorimeter depth. The fit is found to provide an adequate description of the data and of the position of the shower maximum.

A selection of the data recorded at lower energies at DESY (1–6 GeV) and CERN(6–45 GeV) are shown in Figure 41. These illustrate the expected increase as a function of beam energy in both longitudinal position of the shower maximum, and also of the total extent of the shower. By way of demonstrating the compatibility of these two sets of data, Figure 41 compares data recorded at both CERN and DESY with a 6 GeV e^-. These data are found to be completely consistent and therefore the data recorded at both CERN

and DESY are considered together. The position of the shower maximum is extracted from the parametrisation at each energy considered and shown in Figure 42. The depth is found to grow logarithmically with beam energy and data from the two different test beam runs are compatible.

Next in Figure 43, the variation of the shower maximum position is studied at various angles of incidence for a single beam energy of 30 GeV. There is some deviation observed for the dataset with a beam angle of 0^o from the expected behaviour. This is plausibly due to the lack of any correction for the reduction in efficiency near to the inter-wafer gap regions. For non-normal incidence this effect cannot be avoided by simply rejecting events as the shower will impinge on such a region in at least some fraction of the layers. Overall, the shower maximum varies as the cosine of the incoming beam trajectory, i.e. proportional to the amount of the absorber material traversed.

The final study carried out is to estimate the amount of energy not measured in the DESY data owing to the absence of several instrumented layers in the most downstream third of the calorimeter. This missing energy is calculated from the longitudinal shower parametrisation. As can be seen in Figure 44 the missing energy rises with increasing beam energy.

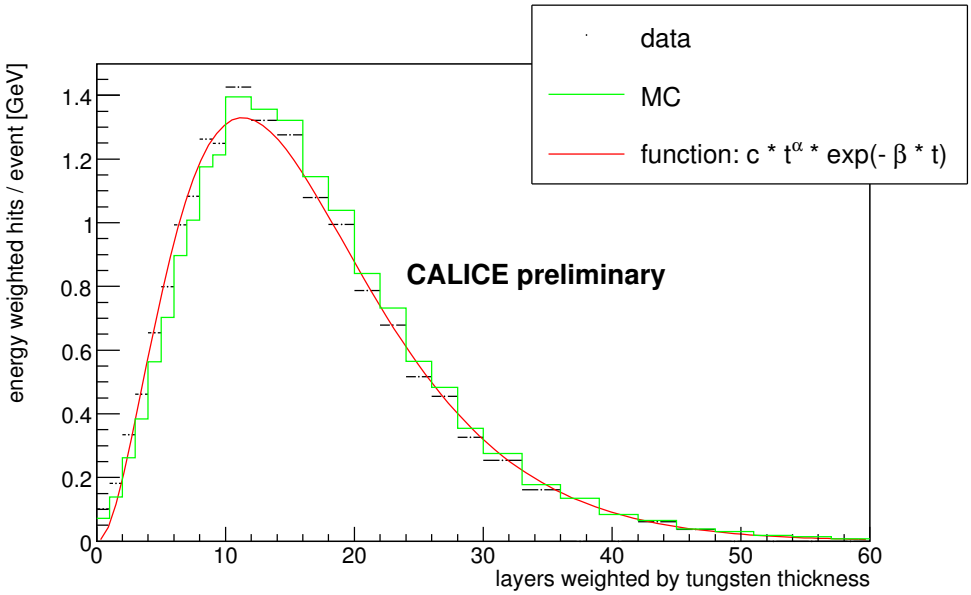

Figure 40: *Longitudinal shower profile obtained from 20 GeV e^- beam at CERN, measured in the CALICE ECAL. The data are represented by points with statistical uncertainties and the GEANT4 Monte Carlo simulation by the histogram. Our preferred parametrisation of the shower profile is given as a smooth curve.*

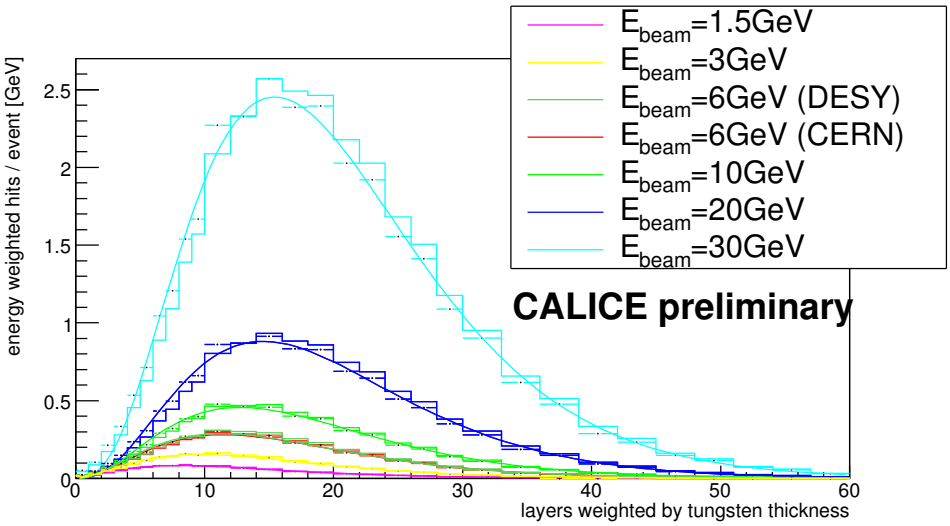

Figure 41: *Longitudinal shower profile from runs at CERN and at DESY with several energies measured in the CALICE ECAL. As in Figure 40 the data are represented by points with statistical uncertainties and the GEANT4 Monte Carlo simulation by the histogram. The parametrisation of the shower profile is the same as in the previous figure.*

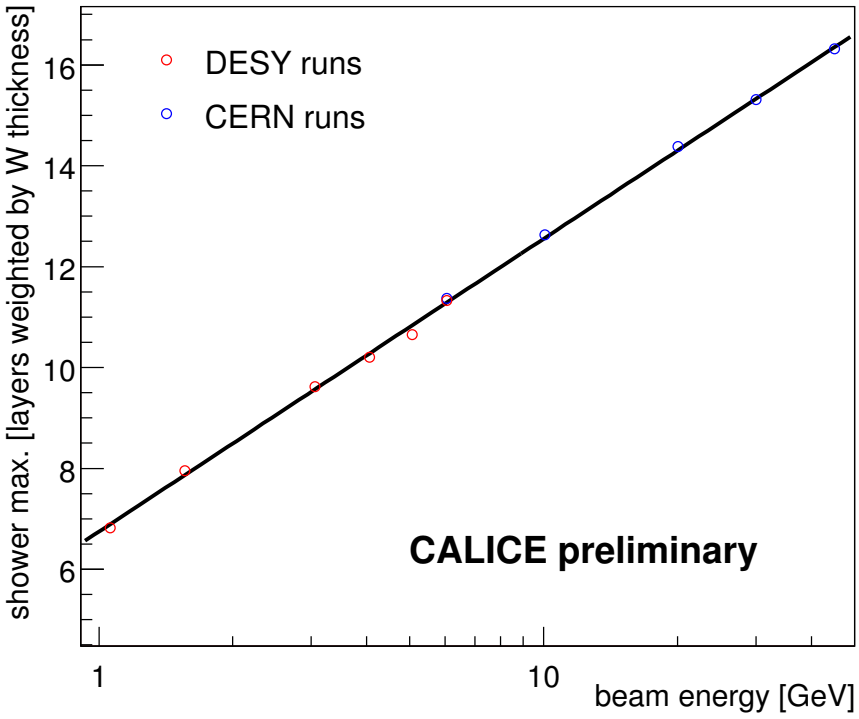

Figure 42: *Shower maximum obtained from fitted curve versus beam energy. The shower maxima are proportional to the logarithm of the beam energy. For a beam energy of 30 GeV data samples at several beam angles are available.*

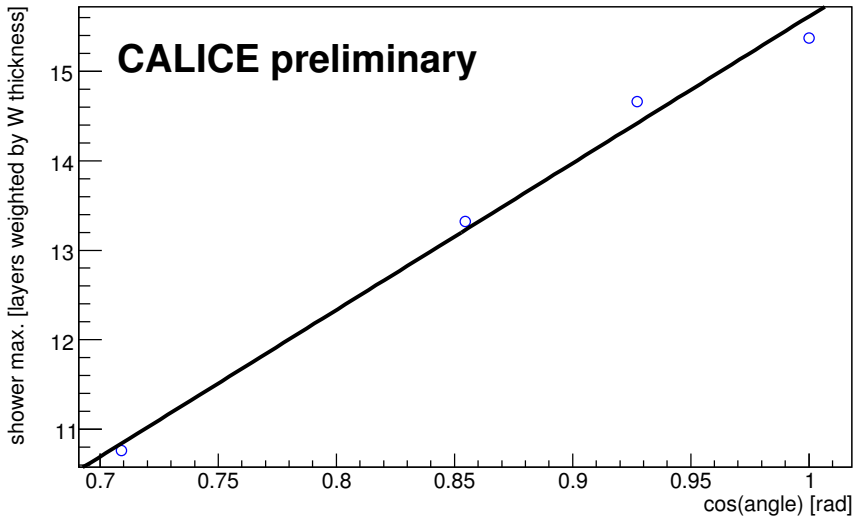

Figure 43: *For a beam energy of 30 GeV data samples at several beam angles are available. These data follow the cosine of the beam angle, which is proportional to shower depth in the calorimeter.*

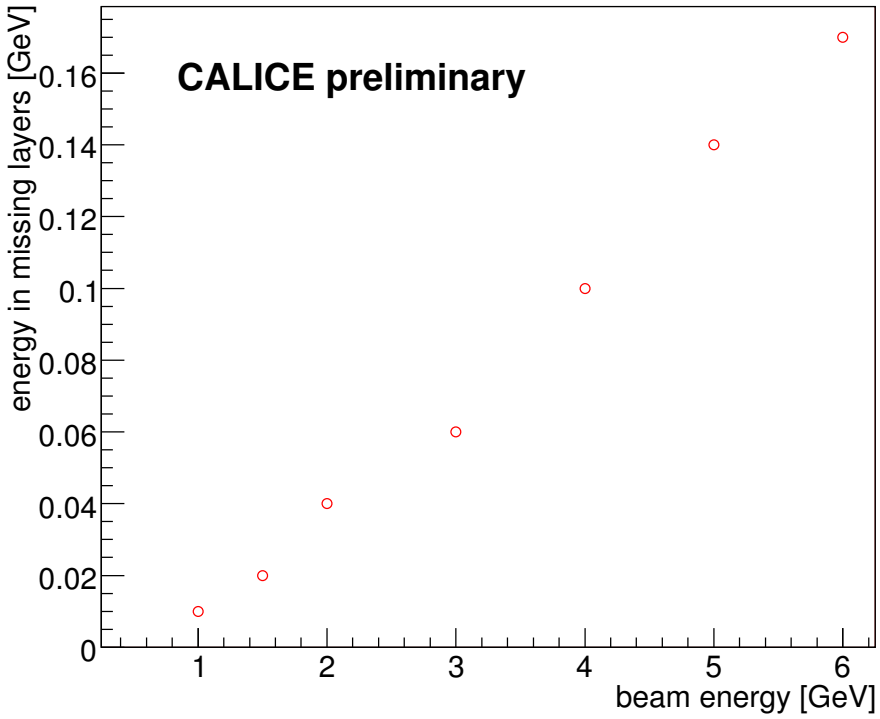

Figure 44: *Missing energy in the missing layers of the DESY runs estimated with the help of the longitudinal shower parametrisation.*

7.3 Transverse shower profile

One of the key issues in the development of a particle flow calorimeter is not only to have fine transverse and longitudinal granularity but also to achieve the smallest possible effective Molière radius, a measure of the visible transverse size of the electromagnetic showers, in order to provide the best possible shower separation and so to have excellent pattern recognition capability. It requires the use of a very dense absorber, such as tungsten which has a Molière radius (R_M) of about 10 mm, and the minimisation of the gaps between the absorber layers of the calorimeter.

The data recorded with the prototype electromagnetic calorimeter during test beam runs with electrons enable us to measure the transverse size of the showers for different energies and impact points. A typical set of results is depicted in Figure 45 and 46. Figure 45 shows the fraction of signal contained within a cylinder centred on the shower axis versus the cylinder's radius for 3 GeV e^- events at normal incidence. For 90% and 95% levels of signal containment the event distribution with respect to the radius is shown in Figure 46(a)-(c) for beam with average impact points around the centre, (a), edge, (b), and corner, (c), of wafers, respectively. The results for the various energies and impact positions studied are summarised in Figure 47. The points correspond to the peak position of each radius distribution. At 90%(95%) shower containment the corresponding radius, often quoted as 1 R_M, is about 20(28) mm when the beam is hitting the front face of the calorimeter around a wafer's centre. It degrades further by about 2 mm at the edge or corner of wafers due to the dead space around the borders of the wafers. As already discussed in Section7.1.1 this is also an illustration how the dead space of the detector can affect its performance and of the need to minimise it as much as possible or try to correct it as efficiently as possible.

The first electromagnetic prototype has an interlayer gap that is 2.2 mm thick in order to accommodate the Si pads and PCB. This fact in combination with the prototype's longitudinal segmentation in 10 layers of 1.4 mm thick W followed by 10 layers at 2.8 mm and the last 10 layers at 4.2 mm leads to an effective Molière radius of the detector that is expected to be larger by a factor of about 2 with respect to R_M of solid tungsten. As shown above the results from the test beam studies are in agreement with expectations. R&D effort towards the use of Si pads with integrating readout is under way and will enable us to decrease significantly the interlayer gap and thus the effective Molière radius of the calorimeter.

7.4 Spatial and angular resolution of ECAL

7.4.1 Introduction

The spatial and angular resolution of the ECAL were studied for the DESY data where the beam entered the ECAL at normal incidence. The shower direction and position at the ECAL front face were constructed on an event-by-event basis using a linear fit to the

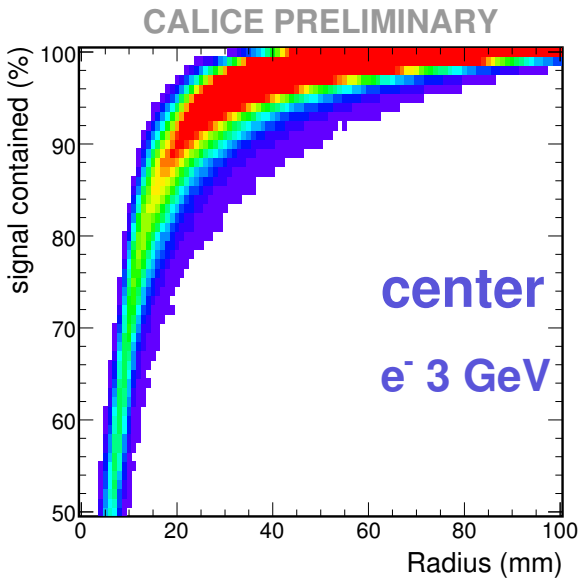

Figure 45: *Fraction of the calorimeter signal contained within given radius around the shower axis of 3 GeV e^- events at normal incidence around the centre of a wafer.*

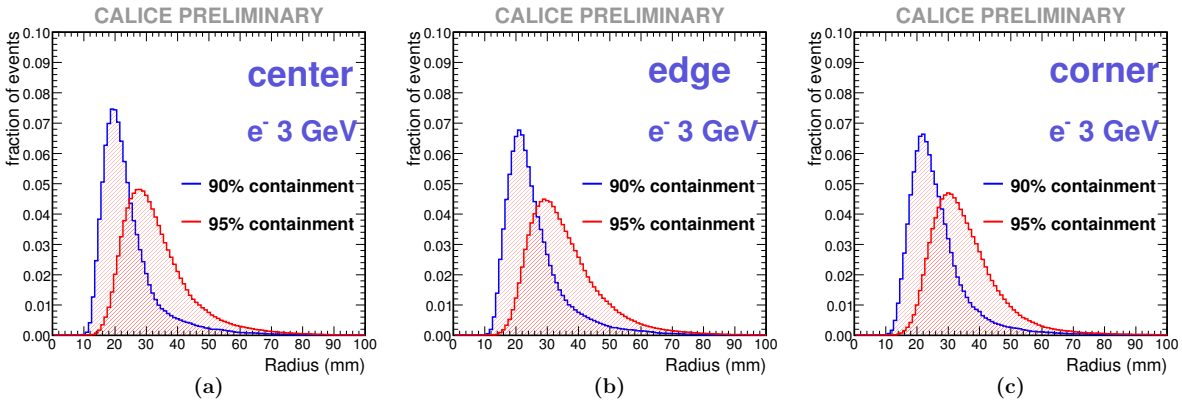

(a) (b) (c)

Figure 46: *Distribution of radii for 90% and 95% signal containment of 3 GeV electrons at normal incidence at the centre, (a), edge, (b) and corner, (c), of wafers, respectively.*

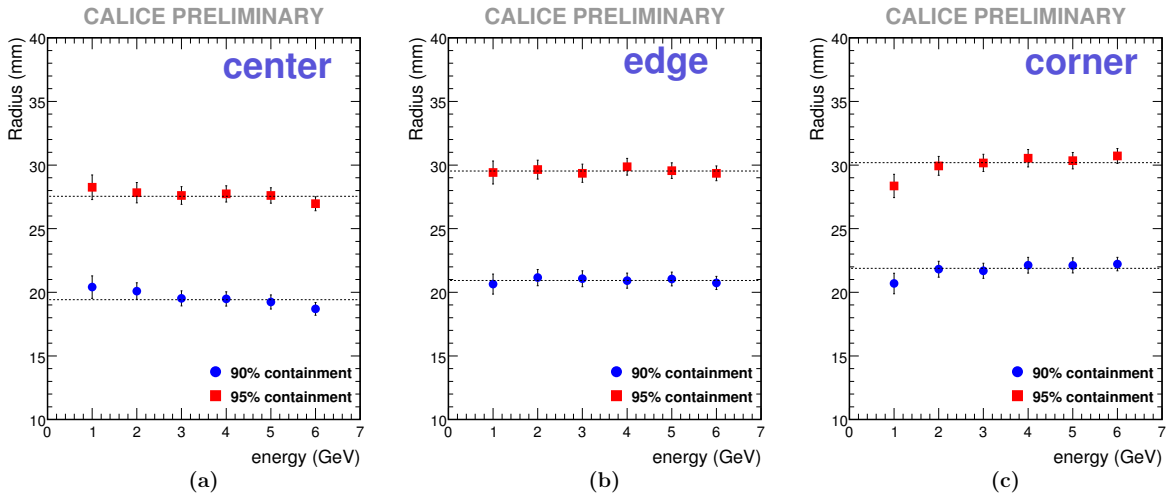

Figure 47: *Radii for 90% and 95% signal containment of electrons at normal incidence at the centre, (a), edge, (b), and corner, (c), of wafers, respectively, and for 1 to 6 GeV incident energy. (Lines shown to guide the eye)*

shower positions in each layer for the x and y coordinates separately. This was compared with the position and angle as measured by the tracking system.

7.4.2 Linear fit to shower

The shower position in each layer of the ECAL was taken to be the energy-weighted position of the hits in that layer

$$\boldsymbol{r}_s = \frac{\sum_i E_i \boldsymbol{r}_i}{\sum_i E_i} \tag{1}$$

where $\boldsymbol{r}_i$ is the centre of the pad with hit i, and E_i the hit energy. A linear two-parameter chi-squared fit was performed to the layer positions to give a shower position and direction.

Such a fit requires a error matrix and this was determined from simulated events for each beam energy separately. The error matrix was constructed by projecting the exactly-known simulation particle into the ECAL and finding the impact point at each layer. This was then compared with the energy-weighted position as defined above. The differences between these positions were used to calculate an error matrix for the shower in each layer in both x and y, including layer-to-layer correlations using

$$e_{ij} = \frac{\sum (\Delta c_i \Delta c_j)}{N - 1} \tag{2}$$

where e_{ij} is the error matrix element for layer/coordinates i and j, Δc_i is the difference in positions in layer i and the sum is over all N events in the simulation. The range of i and j is $0 - 47$ where 0 is layer $1x$, 1 is layer $1y$, 2 is layer $2x$, etc. It was found that the error submatrices for x and y were only very weakly correlated, as expected as the ECAL pads are aligned with those coordinates, so the fit was performed for x and y independently.

Hence, two 24×24 error matrices were used in two separate fits rather than one 48×48 error matrix in a combined fit in x and y.

The fit itself was performed by minimising the chi-squared function

$$\chi^2 = \sum_{ij} \left[x_{si} - p_0 - p_1(z_i - z_f)\right] W_{ij} \left[x_{sj} - p_0 - p_1(z_j - z_f)\right] \tag{3}$$

where x_{si} is the x coordinate of the energy-weighted position in layer i, p_0 and p_1 are the fit parameters, z_i is the z position of layer i, z_f is the z position of the ECAL front face and W is the weight matrix, i.e. the inverse of the error matrix e. The parameter p_0 corresponds to the shower position on the ECAL front face while p_1 is the gradient of the shower direction in the $x - z$ plane, i.e. $p_1 = \tan\alpha$ for angle α. For small angles, $p_1 \approx \alpha$. An identical expression holds for the y coordinate fit.

Due to the threshold applied to each energy, the finite shower depth, and dead regions in the ECAL, not every layer gave a hit in every event. The error matrix used in these cases was the submatrix with the layers eliminated where no hits were found. The weight matrix had to be re-evaluated by inverting the resulting error matrix for every such combination. In addition, two layers (2 and 13) were found to have significant numbers of bad channels and were excluded from the fit. Hence, the maximum number of layers used in the fit was 22.

7.4.3 Track reconstruction

The shower position was compared with the track reconstructed using the drift chambers. All drift chamber hits within a very loose fiducial cut range were used as candidates for the track fit and the tracking was done for x and y independently.

For each coordinate, all possible combinations of hits in three or four layers were considered and a separate track fit performed for every such combination. The track fit was a chi-squared fit to the drift chamber position in each of the three or four layers. The error matrix was again determined from simulation in a similar way to the shower fit. The known particle position was extrapolated back from the ECAL front face and compared with the true hit positions in the tracking chambers. The intrinsic chamber resolution was then added as an uncorrelated addition to the diagonal elements of the error matrix. By extrapolating the known particle position from the ECAL front face, the effects of all the scattering material between the tracking system and the ECAL (as well as the material within the tracking system) were included in the fit error matrix. A different matrix was determined for each beam energy.

The track fits to all four-hit combinations were compared and the one with the largest chi-squared fit probability was retained, if the probability was greater than 0.1. Any tracks which used the same hits as this track were then eliminated from further consideration. The remaining four-hit tracks were then compared and again the track with the largest probability exceeding 0.1 was retained. As before, any tracks sharing the same hits were

then excluded. This continued until there were no further four-hit tracks satisfying the probability criterion. Note, the first track found in the event has the best fit chi-squared.

A similar algorithm was then applied to the three-hit tracks, where the requirement on the probability was loosened to 0.01. However, only tracks with four hits were used in the following analysis.

7.4.4 Track systematic errors

Knowledge of the resolution of the tracking system was required in order to determine the ECAL resolution. Hence, uncertainties in the tracking resolution directly affect the estimate of the ECAL performance. The tracking resolution systematic errors arise from limited simulation statistics, residual misalignment of the tracking system, imperfect modelling of the scattering material in the beam line, uncertainties in the intrinsic drift chamber resolution and imperfect modelling of the tracking chamber backgrounds. The differences between the systematic errors in x and y were found to be negligible.

The resolutions were determined from simulation with approximately 100k events per energy, resulting in a non-zero statistical error on the resolution. The residual misalignment errors were estimated by reconstructing simulated events with the tracking chamber drift velocity increased by 5% compared with the value used to generate the hits. Imperfect modelling of the beam line material in the simulation will result in the scattering contribution to the track fit error matrix being incorrect. The effect of this was estimated by scaling the scattering material error matrix by $\pm 10\%$. The effect of the intrinsic resolution was estimated by varying the measured $400\,\mu$m point resolution by $\pm 50\,\mu$m. The chamber backgrounds were modelled by adding random hits at a rate consistent with that observed in the data. The systematic error due to the background was evaluated by scaling the simulated background by $\pm 50\%$. A summary of the tracking systematic errors is shown in table 6.

Table 7 shows the track resolutions and errors for the extrapolated projection on the ECAL front face and for the track gradient for each beam energy. It can be seen that the values for the resolutions in y are slightly better than for x. This is because all the chambers have the y measuring volume downstream of the x volume by 50 mm. This should be compared with the distance from the last chamber to the ECAL front face, which is of order 600 mm, so there is a shift of $\sim 10\%$ between x and y. This shift means the y measurements are systematically closer to the ECAL and so give better resolution.

7.4.5 Position and angle resolutions

Runs with the beam hitting the ECAL at normal incidence and centred on a wafer were used, specifically runs in the range 230097 to 230104. These covered all DESY beam energies except 1.5 GeV. The first four-hit track (specifically the one with the best chi-squared) found in each event was extrapolated to the ECAL front face and the difference

	Beam Energy (GeV)					
Source of error	1.0	2.0	3.0	4.0	5.0	6.0
Position resolution (mm)						
Simulation statistics	0.02	0.01	0.01	0.01	0.01	0.01
Residual misalignment	0.16	0.09	0.06	0.04	0.02	0.02
Material modelling	0.13	0.07	0.04	0.03	0.03	0.02
Intrinsic resolution	0.05	0.05	0.05	0.05	0.05	0.05
Background rate	0.05	0.02	0.02	0.02	0.01	0.01
Total systematic error	0.22	0.12	0.09	0.07	0.06	0.06
Angle resolution (mrad)						
Simulation statistics	0.02	0.01	0.01	0.01	0.01	0.01
Residual misalignment	0.02	0.02	0.01	0.00	0.00	0.00
Material modelling	0.23	0.12	0.08	0.06	0.05	0.04
Intrinsic resolution	0.03	0.02	0.02	0.02	0.02	0.02
Background rate	0.14	0.04	0.02	0.02	0.01	0.01
Total systematic error	0.27	0.13	0.09	0.07	0.06	0.05

Table 6: *Systematic errors on the track resolutions valid for both x and y coordinates. The total systematic error is taken as the quadratic sum of the individual contributions.*

	x		y	
Beam Energy (GeV)	Position (mm)	Angle (mrad)	Position (mm)	Angle (mrad)
1.0	1.68 ± 0.22	2.48 ± 0.27	1.57 ± 0.22	2.41 ± 0.27
2.0	1.00 ± 0.12	1.34 ± 0.13	0.98 ± 0.12	1.30 ± 0.13
3.0	0.81 ± 0.09	0.92 ± 0.09	0.79 ± 0.09	0.90 ± 0.09
4.0	0.72 ± 0.07	0.73 ± 0.07	0.69 ± 0.07	0.72 ± 0.07
5.0	0.66 ± 0.06	0.62 ± 0.06	0.65 ± 0.06	0.61 ± 0.06
6.0	0.60 ± 0.06	0.53 ± 0.05	0.59 ± 0.06	0.52 ± 0.05

Table 7: *Track position and angle resolutions resulting from the track fit.*

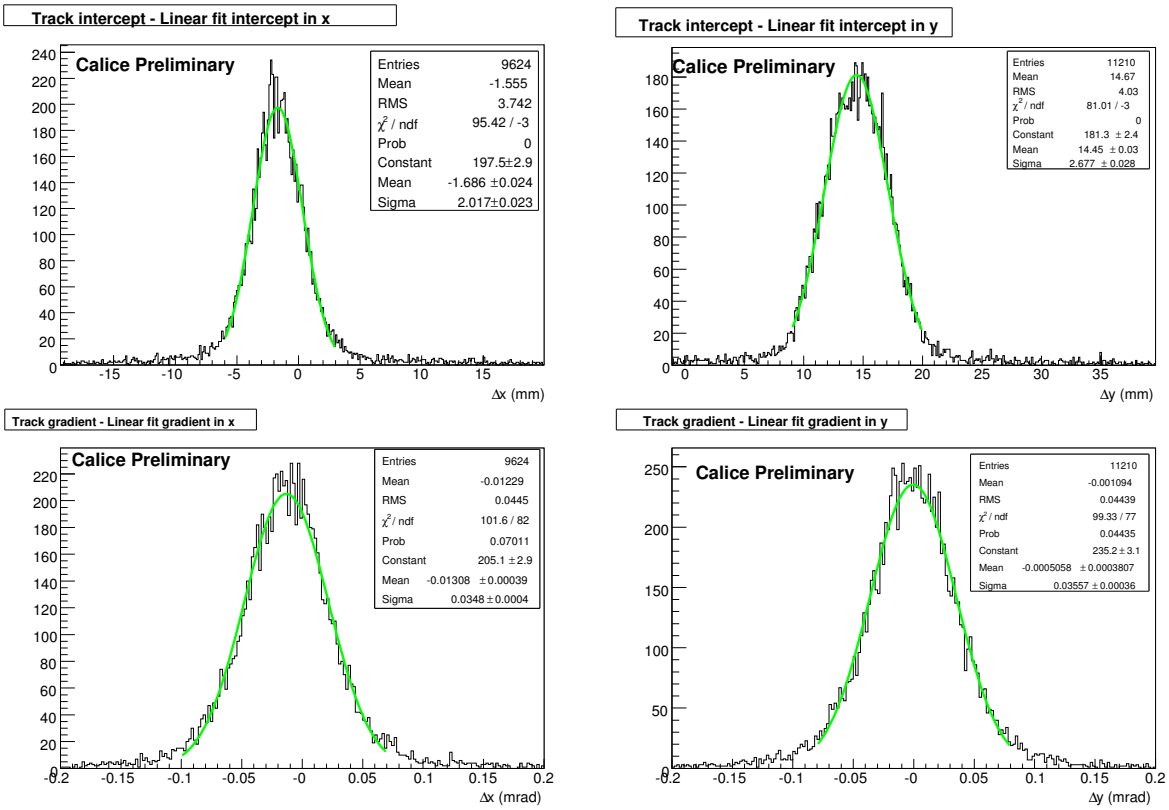

Figure 48: *Difference between the reconstructed shower and track for a) the x coordinate at the ECAL front face, b) the y coordinate, c) the angle tangent in the x direction and d) the angle tangent in y. The data are from a 6 GeV beam energy.*

between the shower fit position and the track position was found, again for x and y independently. The difference between the shower and track angle tangent was also found. An example is shown in Fig. 48 for data from a run with a beam energy of 6 GeV. The offset in the peak positions in Figs. 48(a,b) reflects a displacement in the coordinate systems used, and has no effect on the resolution extracted from the width; similarly the offset in Fig. 48(c) reflects a small rotation of the ECAL with respect to the beam direction.

The width of the distribution of the difference between the shower and track position (or angle tangent) was fitted with a Gaussian for each beam energy. This width has contributions both from the shower and the track errors. These widths, together with the resulting ECAL resolutions, are given in tables 8 and 9. The analysis was also performed using simulated events. These resolutions are also given in tables 8 and 9.

The position and angle resolutions are shown in Fig. 49 as a function of the beam energy. The data points shown include both the statistical and systematic errors, as given in tables 8 and 9. The MC statistical errors are not shown but would be mainly negligible on the scale of this plot. There is reasonable agreement between the data and the simulation for the higher energies, but the data have a systematically worse resolution at lower

Beam Energy (GeV)	Data		Simulation	
Position resolutions in x (mm)				
	Track-ECAL Difference	ECAL Resolution	Track-ECAL Difference	ECAL Resolution
1.0	3.26 ± 0.03	2.79 ± 0.12	3.12 ± 0.03	2.63 ± 0.04
2.0	2.66 ± 0.03	2.46 ± 0.06	2.53 ± 0.02	2.32 ± 0.02
3.0	2.35 ± 0.02	2.21 ± 0.04	2.36 ± 0.02	2.22 ± 0.02
4.0	2.27 ± 0.03	2.15 ± 0.04	2.24 ± 0.02	2.12 ± 0.02
5.0	2.15 ± 0.05	2.05 ± 0.06	2.13 ± 0.02	2.03 ± 0.02
6.0	1.99 ± 0.03	1.90 ± 0.04	1.95 ± 0.02	1.86 ± 0.02
Angle resolutions in x (mrad)				
	Track-ECAL Difference	ECAL Resolution	Track-ECAL Difference	ECAL Resolution
1.0	72.3 ± 0.7	72.3 ± 0.7	65.3 ± 0.8	65.3 ± 0.8
2.0	53.9 ± 0.4	53.9 ± 0.4	48.3 ± 0.4	48.3 ± 0.4
3.0	43.1 ± 0.5	43.1 ± 0.5	41.7 ± 0.3	41.7 ± 0.3
4.0	41.1 ± 0.4	41.1 ± 0.4	37.9 ± 0.3	37.9 ± 0.3
5.0	39.5 ± 0.7	39.5 ± 0.7	34.5 ± 0.2	34.5 ± 0.2
6.0	34.8 ± 0.3	34.7 ± 0.3	32.0 ± 0.2	32.0 ± 0.2

Table 8: *Position and angle resolutions in x determined from comparison to the reconstructed tracks, as a function of the beam energy. For the data resolution values, the total of the statistical and systematic errors is given. For all others, only the statistical error is given.*

Beam Energy (GeV)	Data		Simulation	
Position resolutions in y (mm)				
	Track-ECAL Difference	ECAL Resolution	Track-ECAL Difference	ECAL Resolution
1.0	3.98 ± 0.04	3.66 ± 0.11	3.87 ± 0.03	3.54 ± 0.03
2.0	3.33 ± 0.03	3.18 ± 0.05	3.22 ± 0.02	3.07 ± 0.02
3.0	3.01 ± 0.03	2.90 ± 0.04	2.99 ± 0.02	2.88 ± 0.02
4.0	2.88 ± 0.03	2.80 ± 0.04	2.86 ± 0.02	2.78 ± 0.02
5.0	2.79 ± 0.05	2.71 ± 0.05	2.76 ± 0.02	2.68 ± 0.02
6.0	2.68 ± 0.03	2.61 ± 0.03	2.65 ± 0.03	2.58 ± 0.03
Angle resolutions in y (mrad)				
	Track-ECAL Difference	ECAL Resolution	Track-ECAL Difference	ECAL Resolution
1.0	73.7 ± 0.6	73.6 ± 0.6	63.9 ± 0.8	63.9 ± 0.8
2.0	55.0 ± 0.4	55.0 ± 0.4	48.3 ± 0.4	48.3 ± 0.4
3.0	44.3 ± 0.5	44.3 ± 0.5	42.5 ± 0.3	42.4 ± 0.3
4.0	42.2 ± 0.3	42.2 ± 0.3	38.4 ± 0.3	38.4 ± 0.3
5.0	38.6 ± 0.5	38.6 ± 0.5	35.1 ± 0.2	35.1 ± 0.2
6.0	35.5 ± 0.3	35.5 ± 0.3	32.9 ± 0.3	32.9 ± 0.3

Table 9: *Position and angle resolutions in y determined from comparison to the reconstructed tracks, as a function of the beam energy. For the data resolution values, the total of the statistical and systematic errors is given. For all others, only the statistical error is given.*

energies in both position and angle. This pattern suggests an effect which dominates for low energies and which has not been adequately taken into account in the simulation. Table 6 shows how the various systematic effects influence the track resolutions at each energy. One possible explanation is inadequate material modelling, which would mainly influence the resolution at lower energies. There is a total of $\sim 10\%$ of a radiation length of material due to the air, tracking chambers and trigger scintillators upstream of the ECAL in the simulation. Scaling the $\pm 10\%$ error assumed above up to $\sim +30\%$ gives an idea of the scale of the shift which would be needed, so this would correspond to requiring another $\sim 3\%$ of a radiation length of material. This would result in showers starting a little earlier in the data than the simulation currently and there are suggestions of such effects in the studies reported above.

8 Summary

9 Acknowledgements

The work was supported by the grant No 202/05/0653 of the Grant Agency of the Czech Republic.

etc etc.

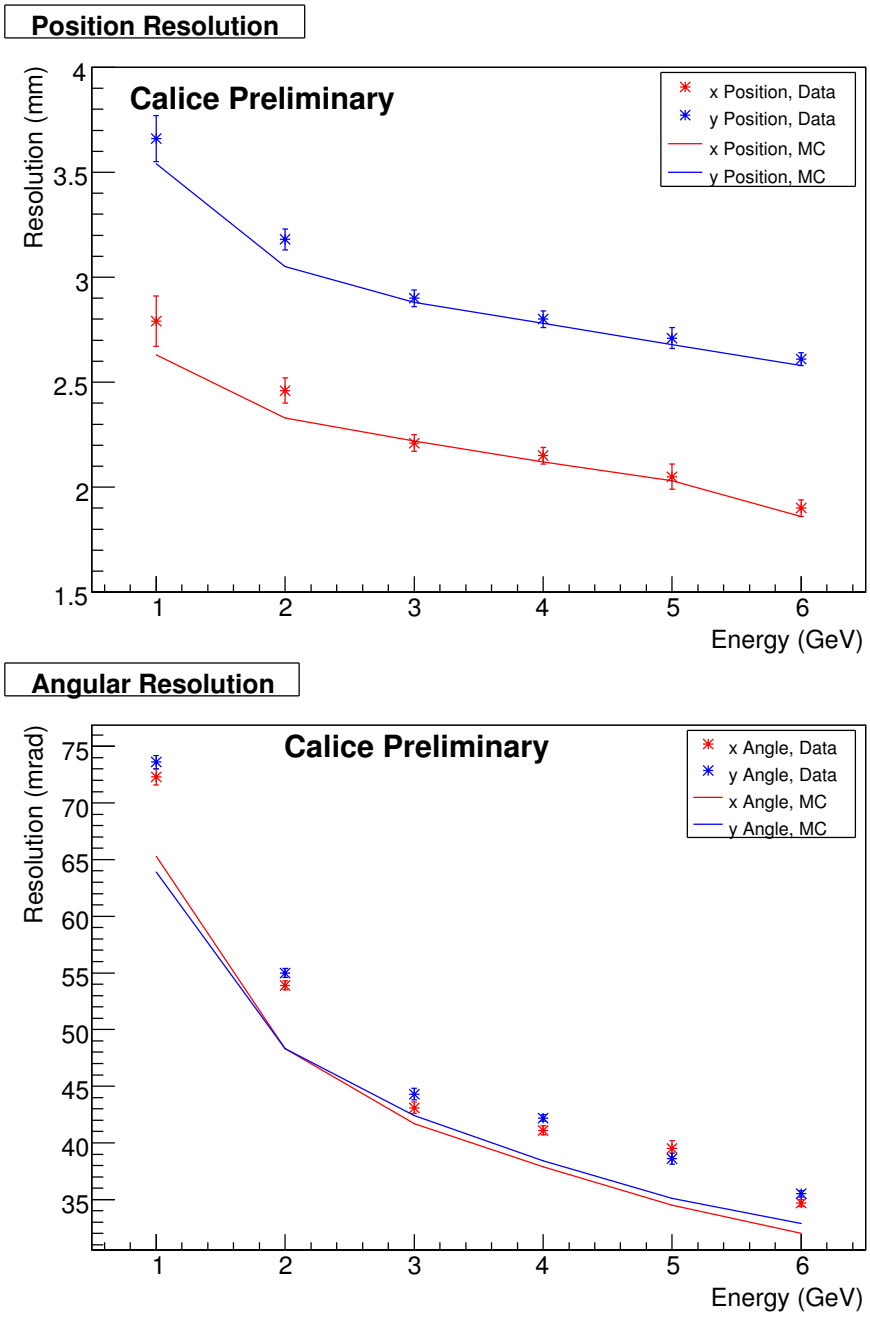

Figure 49: *Resolutions in a) position and b) angle as a function of the beam energy. The data are shown as points with error bars. The simulation expectation is shown by the continuous line.*

References

[1] "Marlin: ".

[2] "LCIO: A Persistency framework for linear collider simulation studies", F. Gaede, T. Behnke, N. Graf, T. Johnson, SLAC-PUB-9992, CHEP-2003-TUKT001, 2003. In the Proceedings of "2003 Conference for Computing in High-Energy and Nuclear Physics (CHEP 03)", La Jolla, California.

[3] "Delay Wire Chambers", J. Spanggaard, SL-Note-98-023 (BI) (1998).

[4] "Geant4 - A Simulation Toolkit ", S. Agostinelli et al., Nuclear Instruments and Methods A 506 (2003) 250-303.

[5] J. Allison et al., IEEE Transactions on Nuclear Science 53 No. 1 (2006) 270-278.

[6] "Mokka - A detailed Geant4 simulation for the International Linear Collider detectors", http://polywww.in2p3.fr:8081/MOKKA.